Electronic Supplementary Material (ESI) for Materials Horizons.

Supporting Information

Oxygen vacancy modulated amorphous tungsten oxide films for fast-switching and ultra-stable dual-band electrochromic energy storage smart windows

Mingjun Chen[a], Xiang Zhang[b,] *, Dukang Yan[a], Jianbo Deng[a], Wenhai Sun[b], Zitong Li[b], Yingjun Xiao[a], Zhenmin Ding[a], Jiupeng Zhao[a,] *, Yao Li[b]

[a]*School of Chemistry and Chemical Engineering, Harbin Institute of Technology, Harbin, 150001, PR China.*

[b]*Center for Composite Materials and Structure, Harbin Institute of Technology, Harbin 150001, PR China.*

[*]*Corresponding author: jpzhao@hit.edu.cn; zhangxhit@hit.edu.cn; yaoli@hit.edu.cn*

Experimental section

Preparation of the oxygen vacancy modulated a-WO_{3-x} and c-WO_{3-x} films

The oxygen vacancy modulated amorphous tungsten oxide (a-WO_{3-x}-O_V) films were prepared by e-beam evaporation using WO_3 particles (99.99% purity). Commercial ITO glass (10 × 40 and 40 × 40 mm^2, 20-50 Ω/square) or quartz (40×40 mm^2) were used as substrates. We selected ITO with a large resistance of 20 to 50 Ω/square due to its higher transmittance in the near infrared (NIR) band (800-2500 nm). In addition, quartz glass substrates are typically used for testing, such as TEM and Raman, to eliminate the interference of ITO substrates. The commercial ITO glass substrates were purchased from Ningbo Nanotech Advanced Materials Co., Ltd. The WO_3 evaporation particles were purchased from Zhongnuo Advanced Material Technology Co., Ltd. Before deposition, the substrates were ultrasonically washed in deionized water, acetone (AR, Aladdin), and ethanol (AR, Aladdin), and subsequently dried in flowing argon gas. The substrate-target distance was 30 cm and the vacuum chamber was pumped below 1.0 × 10^{-3} Pa with 200 ℃ substrate heating. Then oxygen was introduced into vacuum chamber by the mass flow controllers with mass flows of 0 to 10 sccm. A series of a-WO_{3-x}-O_V films with different oxygen vacancy contents were prepared by controlling the mass flow of oxygen (0, 2.5, 5, and 7.5 sccm) during evaporation. The a-WO_{3-x}-O_v Films prepared at different oxygen flow rates of 0, 2.5, 5, and 7.5 sccm were designated as a-WO_{3-x}-O_V-0, a-WO_{3-x}-O_V-2.5, a-WO_{3-x}-O_V-5, and a-WO_{3-x}-O_V-7.5, respectively.

For comparison purpose, the amorphous tungsten oxide without oxygen vacancy

(a-WO_3-10) were acquired under the oxygen-rich atmosphere (the mass flow of oxygen is 10 sccm) and the oxygen vacancy modulated crystalline tungsten oxide (c-WO_{3-x}-O_V-Ar) was prepared by a post annealing process. The detailed parameters of various WO_{3-x} films films during the preparation process are summarized in Table S1. Post annealing process were carried out in a tube furnace. The tube furnace was first purged with pure Ar for 30 min before heating. The films were annealed at 400 ℃ for 2 h with a 1 ℃/ min heating rate and then cooled down naturally to room temperature.

Assembly of the dual-band electrochromic energy storage (DEES) devices

The DEES devices (size: 40 × 40 mm) were assembled by the a-WO_{3-x}-O_V-2.5 film, the NiO film and 1 M PC/$LiClO_4$, which were employed as the cathode, the anode, and the electrolyte, respectively. The NiO anode was prepared by e-beam evaporation similar to that described above. The NiO evaporation particles (99.99% purity) also were purchased from ZhongNuo Advanced Material Technology Co., Ltd. Different from the preparation of a-WO_{3-x}-O_V, the oxygen was not introduced into the vacuum chamber during the deposition of NiO film. Finally, the transparent NiO films were obtained. And 1 M PC/$LiClO_4$ electrolyte was obtained by dissolving 1.06g lithium perchlorate ($LiClO_4$, AR, Aladdin) in 12.04 g propylene carbonate (PC, AR, Aladdin) and stirring at 500 rpm for 4 h. Afterward, 13.10 g ultraviolet (UV) glue (98%, Macklin) was added slowly to the 1 M PC/$LiClO_4$ electrolyte mixture and then stirred 1 h to obtain the transparent quasi-solid-state electrolyte. Finally, the DEES devices were assembled using a-WO_{3-x}-O_V-2.5 film as the cathode, NiO film as the anode, 1 M PC/$LiClO_4$ electrolyte

mixed with UV glue as the quasi-solid-state electrolyte, and a clear 3 M double-sided tape (VHB4010) as the spacer.

Characterizations

The structure, composition and morphology of samples were identified by X-ray diffraction (**XRD**, PANalytical B. V. Model X'pert Pro), **Raman** spectra (Horiba Jobin Yvon LabRAM), High-resolution field emission scanning electron microscopy (**SEM**, Zeiss Supra55) and atomic force microscopy (**AFM**, Dimension Fast Scan). Transmission electron microscopy (**TEM**, FFEI Talos F200S) with corresponding energy dispersive spectroscopy (**EDS**) was used to study the morphology and composition of samples. X-ray photoelectron spectroscopy measurements (**XPS**, Al Kα radiation, PHI 5700 ESCA System) were performed to evaluate the chemical composition of the obtained films. Room-temperature electron paramagnetic resonance (**EPR**, EMX-PLUS) measurements were collected using an Endor spectrometer (JEOL ES-ED3X) at 298 K.

Cyclic voltammetry (**CV**), chronoamperometry (**CA**), galvanostatic charge/discharge (**GCD**) and electrochemical impedance spectroscopy (**EIS**) measurements were carried out on a CHI660E electrochemical workstation (Chenhua, China). Electrochemical properties of the samples were measured in a three-electrode system, where ITO glasses covered by as-prepared samples was employed as working electrodes, a platinum wire as the counter electrodes, an Ag/AgCl electrode as the reference electrodes and 1 M PC-$LiClO_4$ was used as the electrolyte. And electrochemical measurements of the DEES devices were carried out by using a two-electrode system. ITO layer near a-WO_{3-x}-O_V-2.5

layer was connected with the working electrodes, and ITO layer close to NiO layer was connected with counter electrode and reference electrode. In-situ optical transmittance over a wavelength range of 380~1100 nm was measured by Vis-NIR fiber optic spectrometer (MAYA 2000-Pro, Ocean Optics). Ex-situ optical transmittance was measured by a UV-Vis-NIR scanning spectrophotometer (Lambda-950, Perkin Elmer) at the wavelength region of 250-2500 nm.

Simulation test of thermal control performance

The model house with a size of 100 × 100 × 100 mm^2 was made from polyurethane (PU) foam, and a 40 × 40 mm^2 window opened in the front-side of house. The thickness of PU foam is 3 mm, the thermal conductivity is ~0.033 W/(m·K). A DEES device (size: 40 × 40 mm) was installed as the windows. The xenon lamp (HF-GHX-XE-300) was used as heat sources to simulate solar radiation, and two thermocouples were used to measure the temperature of the indoor and window surface under three distinct operating modes: bright mode (+2.0 V), cool mode (-1.2 V), and dark mode (-2.0 V). During testing, the simulated solar light was irradiated vertically on the window and the distance between the xenon lamp and the model house was about 30 cm.

Theoretical calculations

The theoretical calculations were performed with the density functional theory (DFT) and the plane-wave pseudpotential method using generalized gradient approximation (GGA) of Perdew-Burke-Ernzerhof (PBE) functional. The Projector Augmented Wave (PAW) potential was employed to describe the interaction between

valence electrons and core electrons. The diffusion paths and corresponding diffusion energy barriers of Li^+ were calculated by climbing image nudged elastic band (CI-NEB) method with a force-based optimization scheme. In all calculation, an energy cutoff of 400 eV was used for the plane wave expansion of electronic wave function. The force on each atom and the energy convergence criterion of the electronic self-consistency were set to be 0.01 eV/Å and 10^{-5} eV, respectively. The Monkhorst-Pack k-point sampling scheme was used to chosen a gamma-centered 3×2×1 k-point grid in the first Brillouin region. An interface structure model was built along the (2 0 0) surface of the orthorhombic WO_3, in which a vacuum slab of 15 Å was added to separate the interaction between periodic units perpendicular to the plane direction. The oxygen atoms on the surfaces of the slab model were removed to simulate surface oxygen vacancy.

Equation

Equation S1. The calculation of optical transmittance modulation (Δ*T*)

It can be calculated by the following equation:

$$\Delta T = T_b - T_c \quad (1)$$

whereT_b and T_c refer to the transmittance in the bleached and colored states, respectively.

Equation S2-S3. Integrated optical transmittance (T) and integrated solar irradiance transmittance (T') of samples in the VIS light region (380-780 nm), NIR region (780-2500 nm) and total solar irradiation region (sol, 300-2500 nm) at +0.8, -0.2, and -0.8 V.

The calculations were based on these equations:

$$\mathrm{T_{sol}} = \frac{\int \mathrm{T}(\lambda)\mathrm{d}\lambda}{\int \mathrm{d}\lambda} \quad (2)$$

$$T_{sol}' = \frac{\int \mathrm{T}(\lambda)\psi(\lambda)\mathrm{d}\lambda}{\int \psi(\lambda)\mathrm{d}\lambda} \quad (3)$$

where T(λ) is the transmittance at wavelength of λ, and Ψ(λ) is the solar irradiance at 1.5 air mass.

Equation S4-S6. The calculation of Coloration efficiency (CE)

It can be calculated based on the formulas as follows:

$$\mathrm{CE}=\Delta OD/\Delta Q \quad (4)$$

$$\Delta OD=\log(\mathrm{T_b}/\mathrm{T_c}) \quad (5)$$

$$\Delta Q = \int j dt \tag{6}$$

where T_b and T_c refer to the transmittance of the bleached state and colored state, respectively. And j and t are the current density and time derived from CA measurements.

Equation S7. Specific capacitance

The specific capacitance is calculated according to the following equation:

$$\mathrm{C}=\mathrm{I}\Delta t/\mathrm{m}\Delta V \tag{7}$$

where C ($F \cdot g^{-1}$) is the specific capacitance, I (mA), Δt (s), m (mg) and ΔV (V) represent the discharge current, total discharge time, the mass of active materials and potential windows excluding the IR voltage drop, respectively.

Equation S8. Gravimetric capacity

The gravimetric capacity Q (mAh/g) was calculated with the following equation:

$$\mathrm{Q} = \mathrm{I}\Delta t/3.6\mathrm{m} \tag{8}$$

where I (A), Δt (s), and m (g) represent the discharge current, total discharge time and the weight of active materials respectively.

Equation S9-S12. Round-trip energy consumption

The round-trip energy consumption W (mWh/g) was calculated with the following equation:

$$\mathrm{W}_1 = \int_0^{t_1} \mathrm{I}U(t)dt/3.6\mathrm{m} \quad (9)$$

$$\mathrm{W}_2 = \int_{t_1}^{t_2} \mathrm{I}U(t)dt/3.6\mathrm{m} \quad (10)$$

$$\mathrm{W}_3 = \int_{t_2}^{t_3} \mathrm{U}I(t)dt/3.6\mathrm{m} \quad (11)$$

$$\mathrm{W} = \mathrm{W}_1 + \mathrm{W}_3 - \mathrm{W}_2 \quad (12)$$

where *U(t)* is the potential at time of t, *I(t)* is the current at time of t, I (A), U (A), and m (g) represent the discharge/charge current, potential and the weight of active materials respectively. W, W_1, W_2 and W_3 is the net energy consumption of the round-trip, the energy consumption of galvanostatic charging process, the energy consumption of galvanostatic discharging process and the energy consumption of potentiostatic bleaching process, respectively.

Notes

Note 1: Study on the electrochemical mechanism

To elucidate the NIR-selective modulation mechanism of the EC process, the electrochemical behaviours of the a-WO_{3-x}-O_V-2.5 film was investigated. The linear symmetric GCD curves with a slight platform (Fig. S26a) suggest that the charge storage of the a-WO_{3-x}-O_V-2.5 film is governed by the interplay of two different electrochemical mechanisms [1-4], namely: (i) a surface capacitive effect, associated with Li^+ accumulation/adsorption on the surface of the a-WO_{3-x}-O_V-2.5 film; (ii) a diffusion-controlled effect, associated with Li^+ diffusion/insertion into the a-WO_{3-x}-O_V-2.5 film. Thus, the relative weights of these two mechanisms were characterized by meticulous analysis of the CV data at sweep rates from 1 to 10 mV/s (Fig. S26a) according to the following equation:[1, 3]

$$i = av^b$$

where *v* is the sweep rate, *a* and *b* are variables. The value of b is determined from the slope of the plot of log *i* vs. log *v*. Here, *b* = 0.5 is representative of a diffusion-controlled process, while *b* = 1 is indicative of a surface capacitive process.[1, 3] The calculated *b* value is 0.89 according to the oxidation peaks (Fig. S26b), suggesting that the kinetics of the a-WO_{3-x}-O_V-2.5 film are dominated by a surface capacitive process.

To quantitatively distinguish the contributions from the diffusion-controlled process and surface capacitive process to charge storage, we decoupled the values of the measured charge density according to the following equation:[1]

$$i(V) = k_1 v + k_2 v^{1/2}$$

where k_1 and k_2 account for the relative contributions of the surface capacitive and diffusion-controlled processes, respectively. Fig. S26c shows the representative CV curve at a scan rate of 10 mV/s, in which approximately 89.5% of the total accumulated charge originates from the capacitive contribution (shadow area). Meanwhile, the surface capacitive contribution ratio increases from 69.9% to 89.5% when the scan rates are increased from 1 to 10 mV/s (Fig. S26d, e), suggesting that the surface capacitive effect gradually becomes dominant. The desirable surface capacitive behaviour not only contributes to the NIR-selective modulation based on the LSPR effect, but also contributes to the fast electrochemical reaction kinetics[2] and ultra-stable cycling performance.[5] The corresponding sets of CV data for the a-WO_3-10 and c-WO_{3-x}-O_V-Ar films are also provided for comparison in Fig. S27 and S28. As expected, the surface capacitance contribution of the c-WO_{3-x}-O_V-Ar film (Fig. S27) is comparable to that of the a-WO_{3-x}-O_V-2.5 film (Fig. S26), whereas a significantly smaller contribution from surface capacitive charging is observed for the a-WO_3-10 film without any oxygen vacancy: less than 20% of the surface capacitive contribution at a scan rate of 1 mV/s (Fig. S28). Consequently, the results suggest that the oxygen vacancy have a significant effect on

the electrochemical mechanisms of WO_{3-x}, which can enhance NIR-selective modulation through LSPR extinction caused by surface capacitive charging.

Note 2: The calculation of the round-trip energy consumption

During coloring process, the DEES device was charged galvanostatically from 2.0 to −2.0 V at a current density of 4 A/g (Fig. 8d, black line), consuming **162.3** $mWh \cdot g^{-1}$ of energy (W_1, Equation S9). In the bleaching process, the DEES device was first discharged galvanostatically from −2.0 to 0 V at a high current density of 4 A/g (Fig. 8d, black line), releasing **84.7** $mWh \cdot g^{-1}$ of energy in this process (W_2, Equation S10). However, the DEES device could not return to its fully bleaching state by this discharge (the transmittance at 633 nm only increased to 39.0%). A positive voltage (+2 V) was needed for 18 s to restore the device to the fully transparent state (Fig. 8d, blue line). This extra process consumed an additional **21.6** $mWh \cdot g^{-1}$ of energy (W_3, Equation S11). The net energy consumption (W, Equation S12) of the DEES device in an overall electrochromic operation (coloring + bleaching) was therefore reduced to **99.2** $mWh \cdot g^{-1}$ due to efficient energy recycling.

Figures

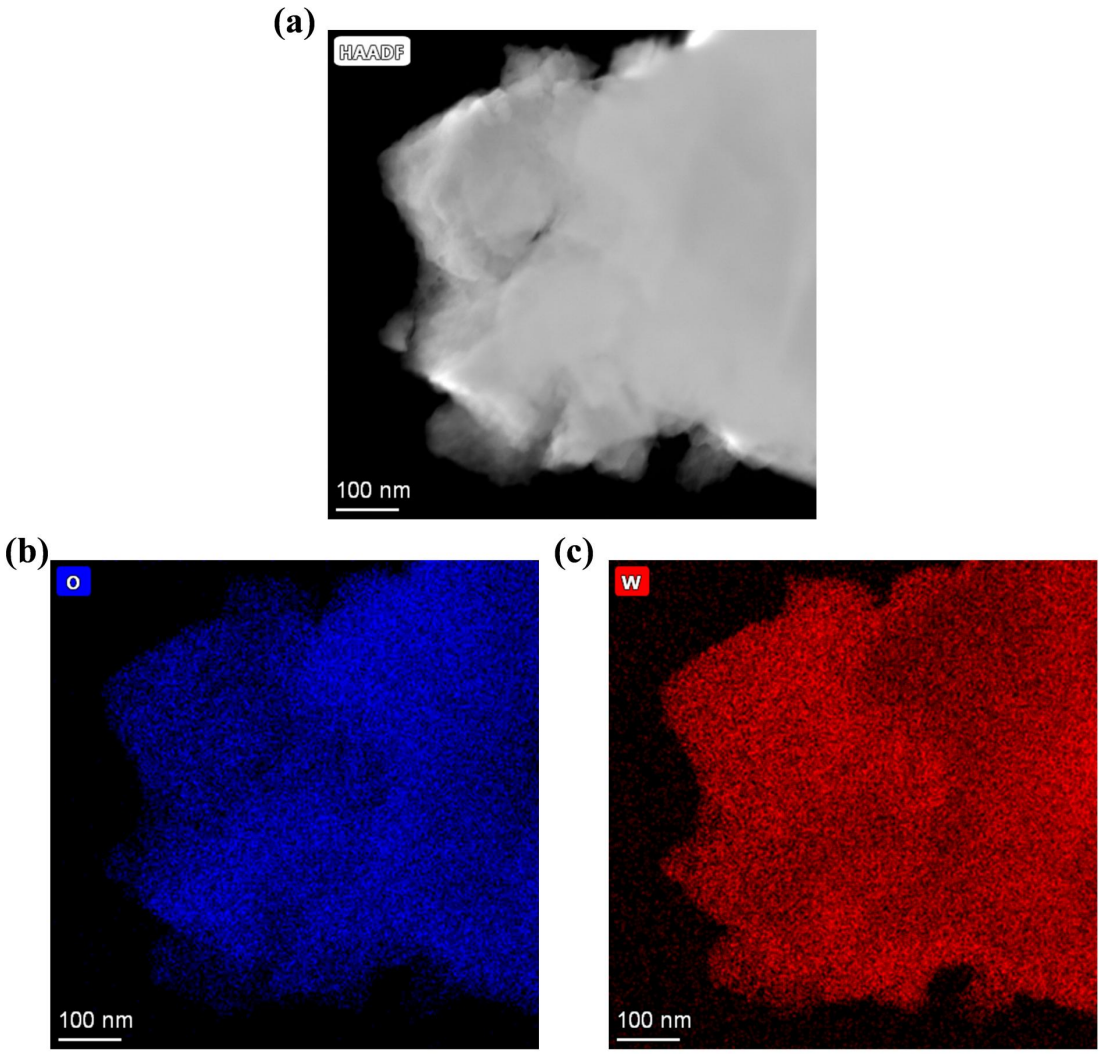

Fig. S1. (a) HAADF-TEM image and EDS mapping images for (b) W and (c) O elements in the a-WO_{3-x}-O_v-2.5.

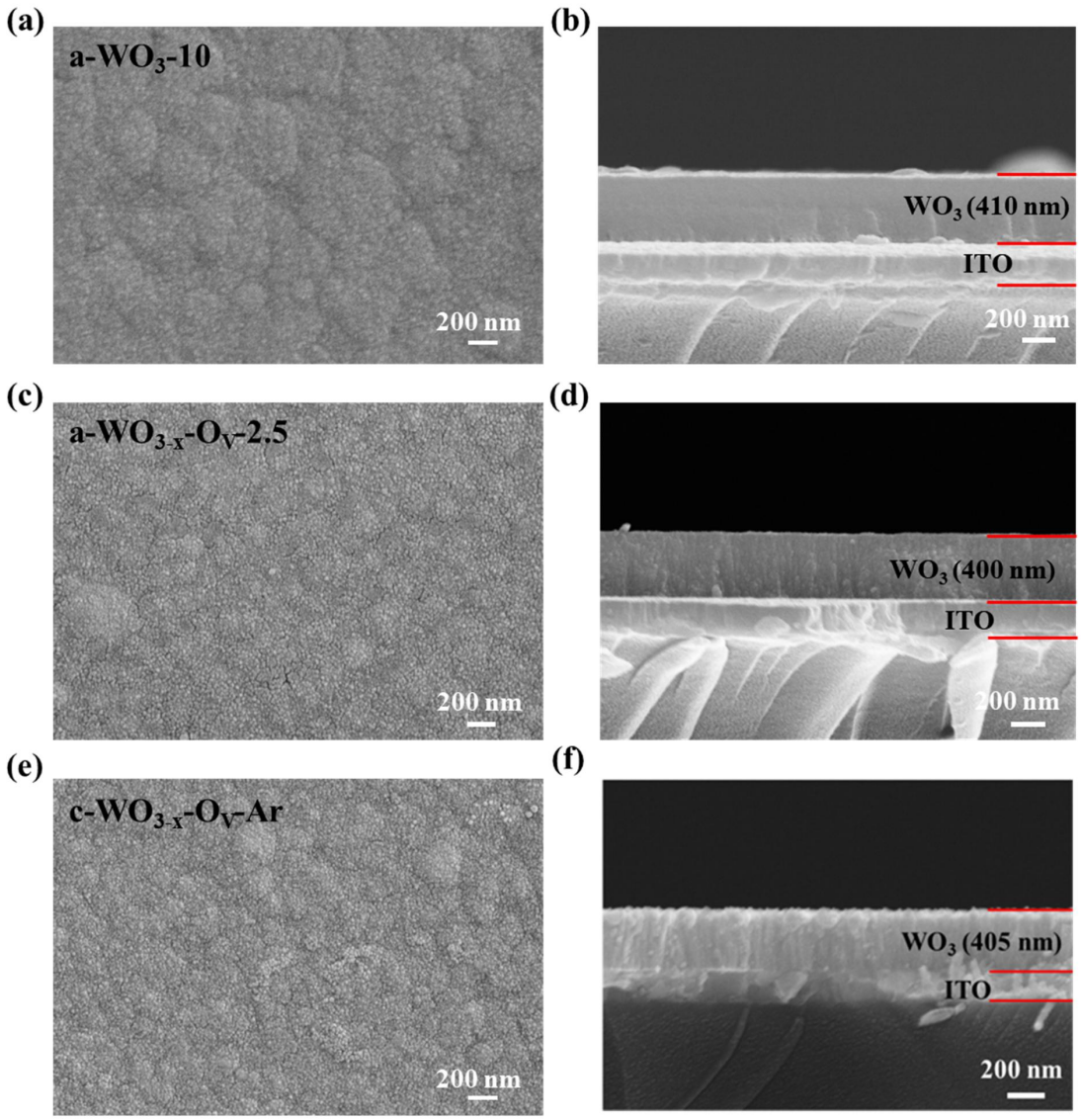

Fig. S2. (a, c, e) Top-view SEM images of the a-WO_3-10, a-WO_{3-x}-O_V-2.5 and c-WO_{3-x}-O_V-Ar samples, respectively. (b, d, f) Cross-sectional SEM images of the a-WO_3-10, a-WO_{3-x}-O_V-2.5 and c-WO_{3-x}-O_V-Ar samples, respectively.

The atomic force microscopy (AFM) with an area of 2×2 μm^2 was used to characterize the surface morphology and roughness of the films, as displayed in **Fig. S2-S3**. The a-WO_{3-x}-O_V-2.5 and c-WO_{3-x}-O_V-Ar samples exhibit porous surface composed of homogeneous nanoparticles, while a-WO_3-10 sample exhibits a surface composed of irregular dense islands.

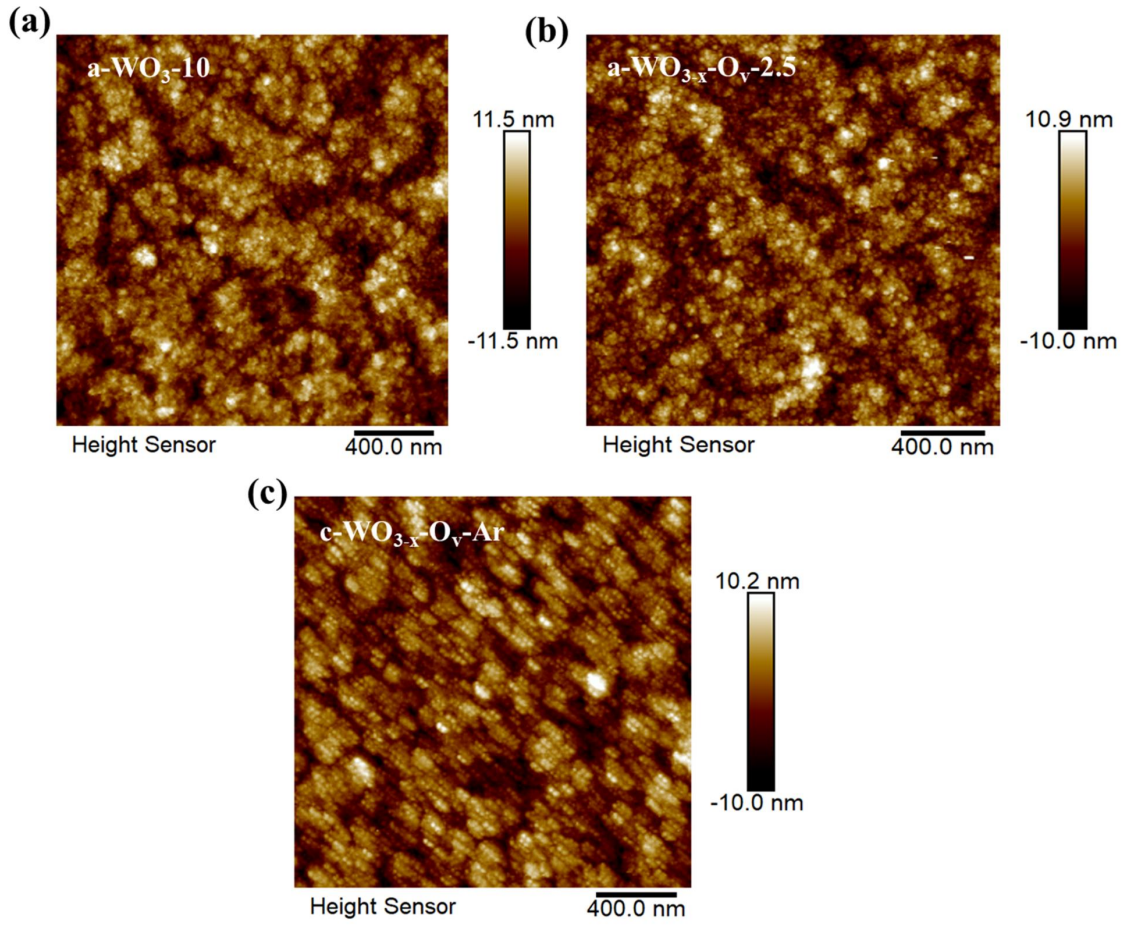

Fig. S3. Two-dimensional AFM images of (a) a-WO_3-10, (b) a-WO_{3-x}-O_V-2.5 and (c) c-WO_{3-x}-O_V-Ar films.

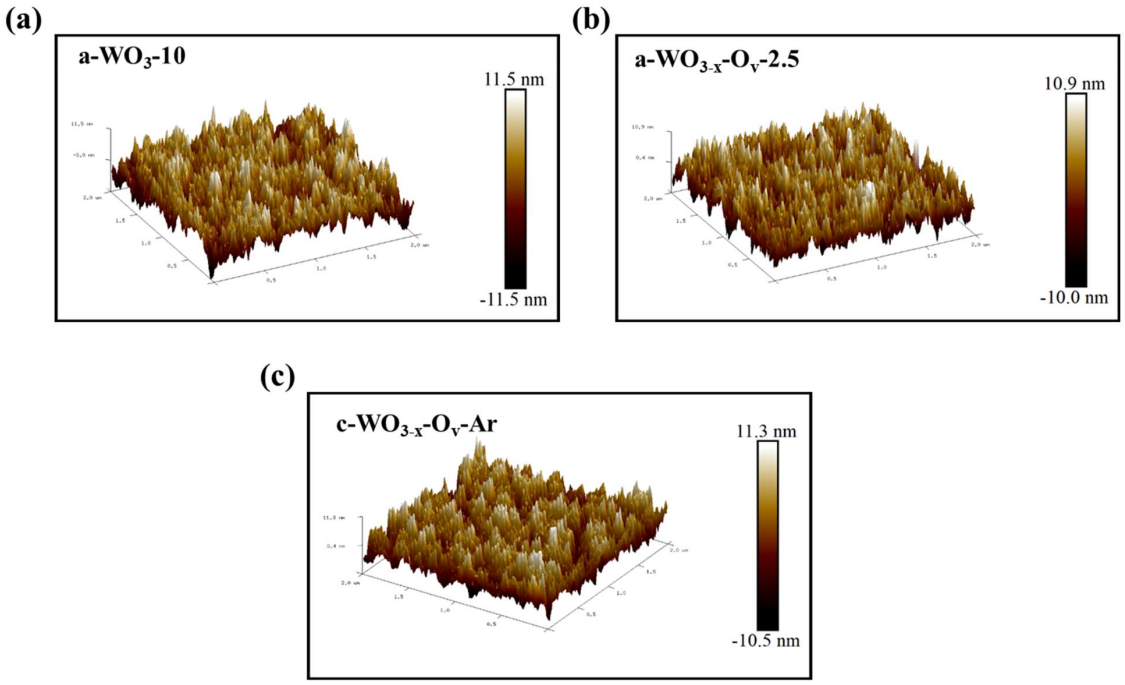

Fig. S4. Three-dimensional AFM images of (a) a-WO_3-10, (b) a-WO_{3-x}-O_V-2.5 and (c) c-WO_{3-x}-O_V-Ar films.

The structure and crystallinity of WO_3 films on ITO coated glass substrate were measured by the X-ray diffraction (XRD). **Fig. S5** shows the XRD patterns of the films prepared at different oxygen flow rates. The diffraction peaks of In_2O_3 (JCPDS card No. 65-3170) can be observed in all films due to all films are deposited on ITO glass substrate [6]. A broad diffraction peak at $2\theta \approx 25^\circ$ can be observed, implying that all WO_{3-x} films are amorphous [7] and the oxygen vacancy has no effect on the crystallization of tungsten oxide.

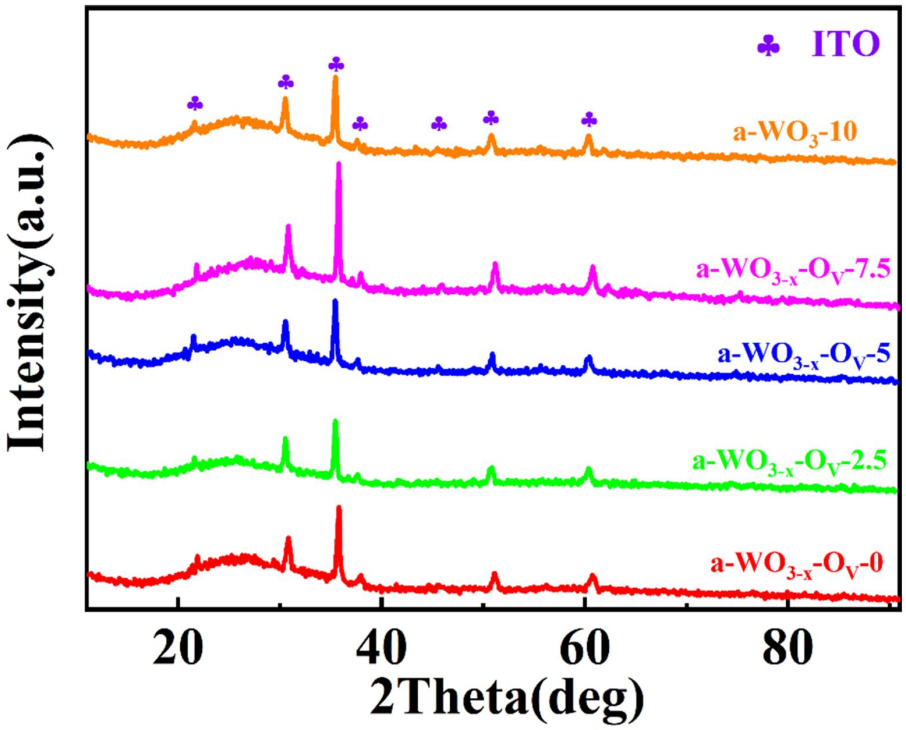

Fig. S5. XRD patterns of the a-WO_{3-x} films prepared at different oxygen flow rates.

The Raman spectra study of WO_{3-x} films was performed on a Horiba Jobin Yvon LabRAM spectrometer equipped with a fiber coupled 532 nm laser. **Fig. S6a** shows the Raman spectra of WO_{3-x} films prepared at different oxygen flow rates. The spectrum of all WO_{3-x} films show a broad peak at 782 cm^{-1} and a relatively sharp peak at 950 cm^{-1}, which have been assigned to the W^{6+}-O bonds and W^{6+}=O stretching mode of terminal oxygen atoms, respectively[8]. These are key characteristics of the amorphous phase, indicating that all WO_{3-x} films are amorphous. In addition, the peaks at 331 and 455 cm^{-1} are assigned to the vibrations of the W^{5+}-O and W^{5+}=O bonds[8]. The existence of low-valent W (W^{5+}) indirectly indicates that oxygen vacancy was likely present on the surface of WO_{3-x} prepared under the hypoxic atmosphere (a-WO_{3-x}-O_V-0, a-WO_{3-x}-O_V-2.5, a-WO_{3-x}-O_V-5, and a-WO_{3-x}-O_V-7.5). In addition, the obvious peak around 1100 cm^{-1} may be attributed to the characteristic peak of ITO glass substrates[7, 9], which also appears in the Raman spectra of bare ITO glass substrates (Fig. S6b).

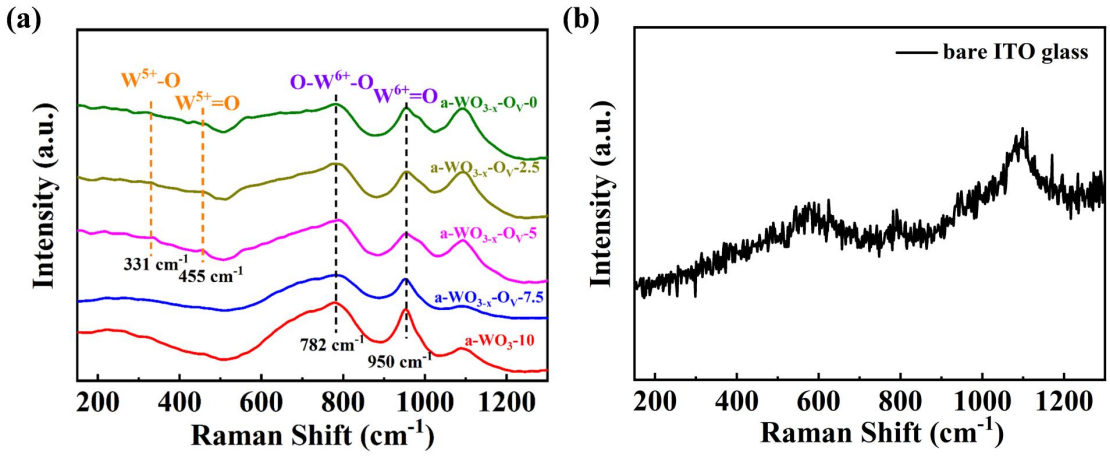

Fig. S6. Raman spectra of the (a) a-WO_{3-x} films prepared at different oxygen flow rates and (b) bare ITO glass substrate.

The composition and chemical bonding states of the WO_{3-x} films were evaluated by the X-ray photoelectron spectroscopy (XPS, PHI 5700 ESCA System) with Al Kα (1486.8 eV) as the X-ray source. **Fig. S7a** depicts the high-resolution spectra of W 4f for the WO_{3-x} films prepared at different oxygen flow rates, in which one pair of doublet peaks of W $4f_{7/2}$ and W $4f_{5/2}$ from W^{6+} states for the a-WO_3-10 film are clearly observed around 35.5 and 37.7 eV, respectively. This result indicates that W is at the highest oxidation state and there is no oxygen vacancy in the a-WO_3-10 film. Interestingly, a different XPS spectrum was obtained for the WO_{3-x} films prepared in the lower hypoxic atmosphere (a-WO_{3-x}-O_V-0, a-WO_{3-x}-O_V-2.5, a-WO_{3-x}-O_V-5, and a-WO_{3-x}-O_V-7.5). The main doublet peaks are not distinctly separated and there is a broadened trend with the bandwidth of W 4f spectrum (**Fig. S7a**), implying multi-peak overlapping in the WO_{3-x} films prepared in a lower hypoxic atmosphere. These spectrums are deconvoluted into two sets of doublet peaks. The first doublet peaks at 35.5 and 37.7 eV ascribes to the W^{6+} and the second doublet peaks at 34.7 and 36.8 eV can be identified as the W^{5+10}. Thus, the existence of W^{5+} indirectly indicates that there may be oxygen vacancy on the surface of WO_{3-x} films prepared in a lower hypoxic atmosphere [11]. Moreover, the area ratios of the W^{5+}/W^{6+} peaks gradually increase with the decrease in oxygen mass flow, indicating that the concentrations of oxygen vacancy in WO_{3-x} films can be controlled by mass flow of oxygen. In the high-resolution XPS spectra of O 1s (**Fig. S7b**), the O 1s spectrum can be deconvoluted to two peaks at 530.5 and 532.3 eV. The main peak around 530.5 eV can be ascribed to the lattice oxygen of W-O bond in the WO_{3-x}. And the additional shoulder

peak around 532.3 eV can be assigned to adsorbed hydroxyl groups species or oxygen ions on the surface, which is probably ascribed to the absorption of H_2O on the surface, resulting from the oxygen vacancy in the WO_{3-x} [11]. The ratios of the adsorbed O in the a-WO_{3-x}-O_V-0, a-WO_{3-x}-O_V-2.5, a-WO_{3-x}-O_V-5, and a-WO_{3-x}-O_V-7.5 films are approximately 13.2%, 16.6%, 18.0%, and 20.4%, respectively, which are higher than that in the a-WO_3-10 film (~13.0%), implying the oxygen vacancy is successfully introduced into the WO_{3-x} films prepared in a lower hypoxic atmosphere (**Fig. S7b**). To further confirm the degree of oxygen vacancy in the samples, we investigated the atomic ratio of O/W and concentrations of oxygen vacancy (V_O) based on W 4f and O 1s XPS high-resolution spectra. The atomic ratio of O/W gradually decreases from 3.0 to 2.74 (The O/W atomic ratio of the a-WO_3-10, a-WO_{3-x}-O_V-7.5, a-WO_{3-x}-O_V-5, a-WO_{3-x}-O_V-2.5, and a-WO_{3-x}-O_V-0 are 3.0, 2.94, 2.88, 2.81, and 2.74, respectively) and the V_O gradually increases from 0 to 8.67% with the decrease of oxygen mass flow (**Fig. S7c**), implying that V_O in WO_{3-x} films can be controlled precisely by the mass flow of oxygen.

Electron paramagnetic spectroscopy (EPR) is a straightforward and advanced technology to detect and characterize oxygen vacancy in materials. Compared to a-WO_3-10 film with negligible EPR signal, the a-WO_{3-x}-O_V-0, a-WO_{3-x}-O_V-2.5, a-WO_{3-x}-O_V-5, and a-WO_{3-x}-O_V-7.5 films exhibit relatively stronger EPR signal intensity at g = 2.0038 and EPR signal intensities gradually weaken with the decrease of oxygen mass flow (**Fig. S7d**). As reported previously, g = 2.003 $\pm$ 0.001 can be attributed to oxygen vacancy on tungsten oxide surfaces [11, 12]. These results also indicate that VO in WO3-x films can be

controlled precisely by the mass flow of oxygen, consistent with the XPS spectra results.

Taken together, these results indicate that oxygen vacancy are successfully introduced into WO_{3-x} films through the facile e-beam evaporation strategy under different concentrations of hypoxic atmosphere, and the concentration of oxygen vacancy can be precisely controlled by the mass flow rate of oxygen during evaporation.

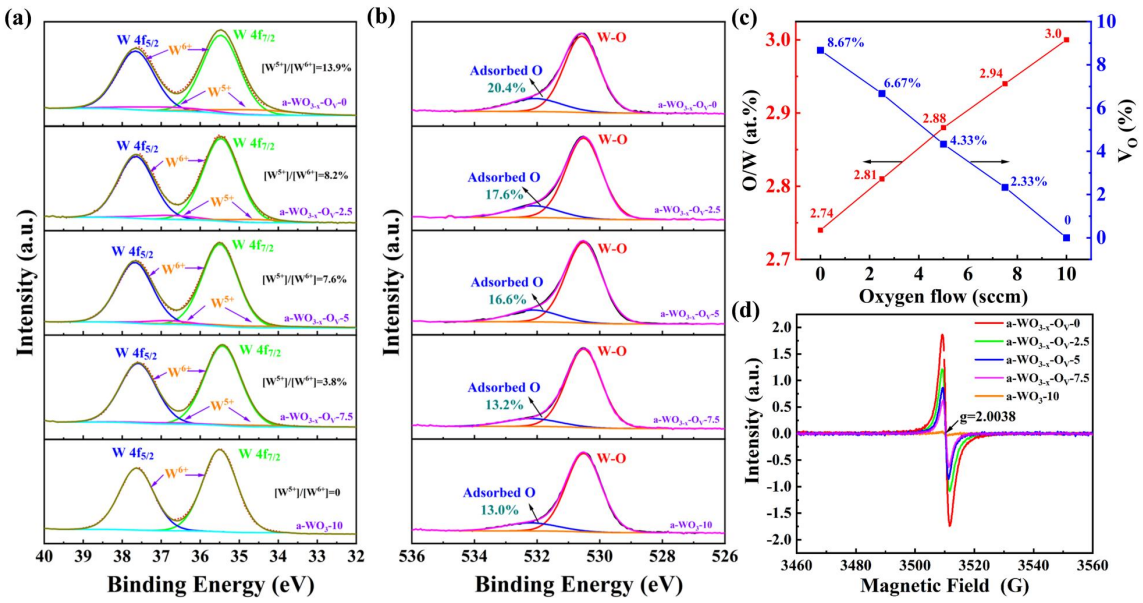

Fig. S7. High-resolution (a) W 4f, (b) O 2p XPS spectra, (c) the atomic ratio of O/W and concentration of oxygen vacancy (V_O), and (d) EPR spectra of the a-WO_{3-x} films prepared at different oxygen flow rates.

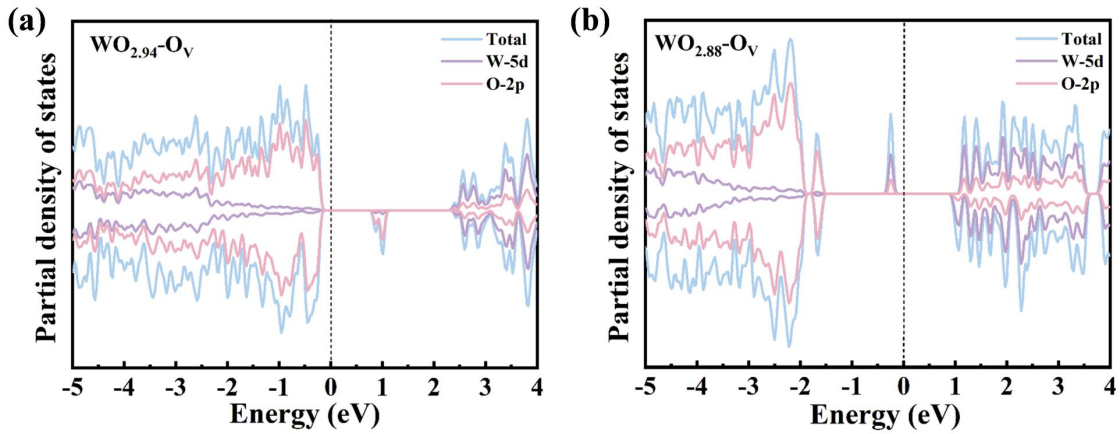

Fig. S8. PDOS patterns of W 5d and O 2p orbitals for the (a) $WO_{2.94}$-O_V and (b)$WO_{2.88}$-O_V.

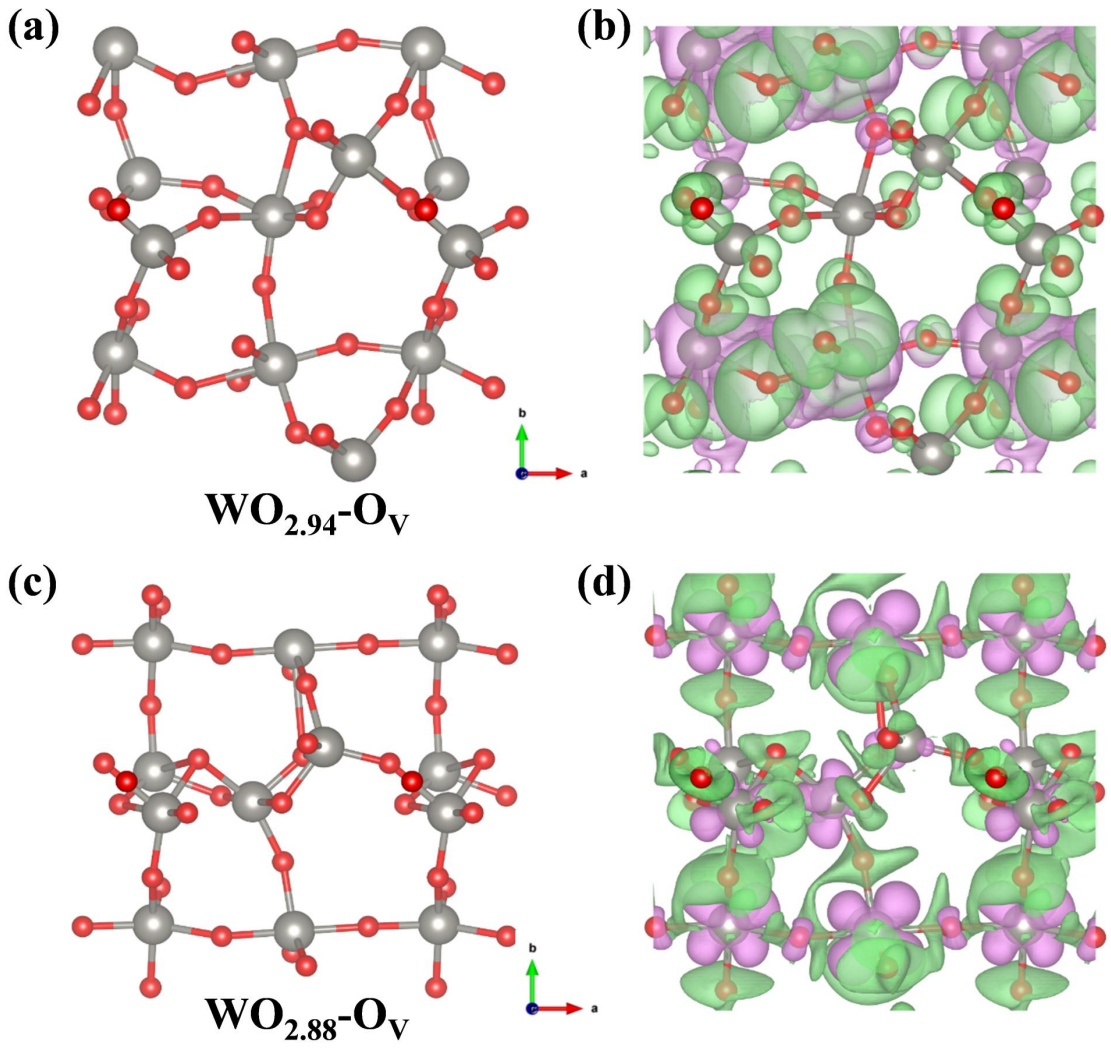

Fig. S9. Computational models and spin electronic density of the (a, b) $WO_{2.94}$-O_V and (c, d) $WO_{2.88}$-O_V.

Spin-up: pink areas, spin down: light green areas.

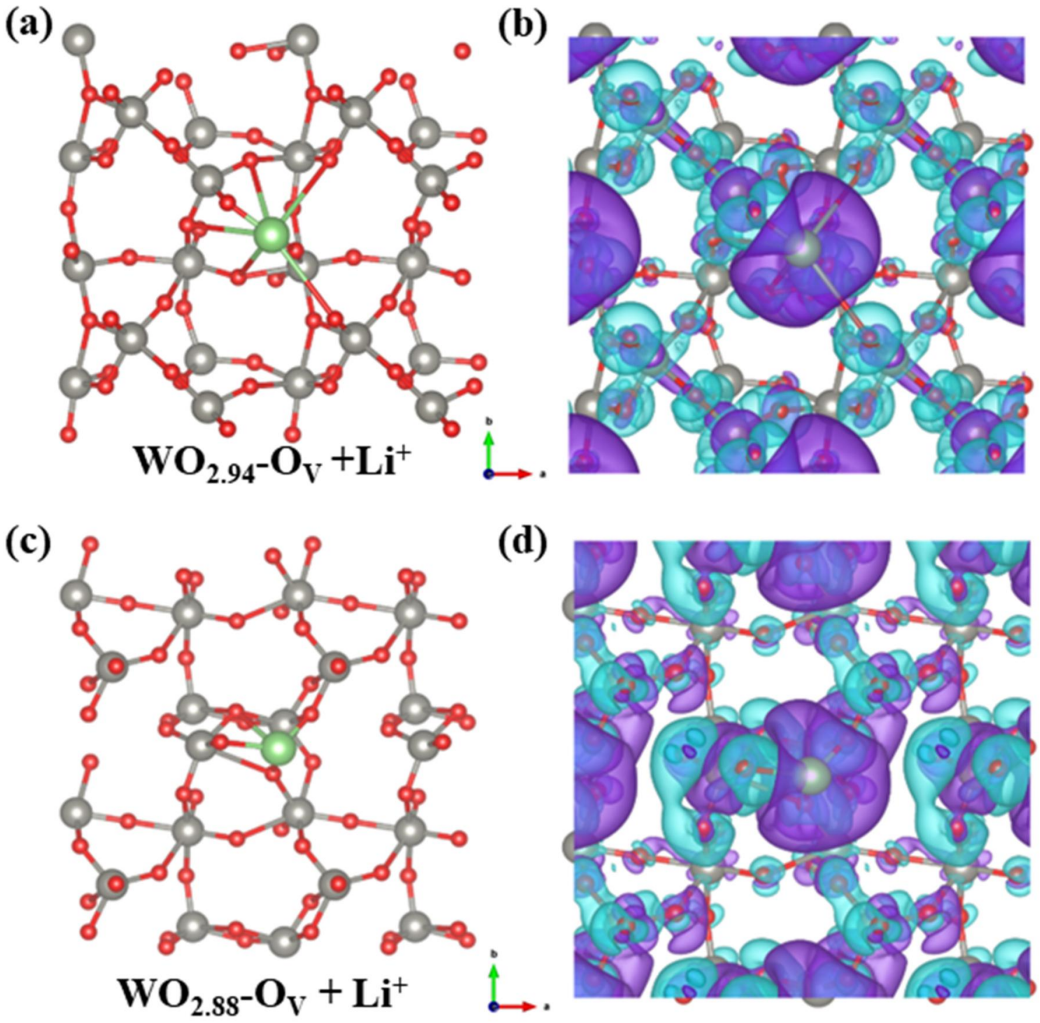

Fig. S10. Computational models and charge density difference (top view) of (a, b) $WO_{2.94}$-O_V with intercalated Li^+ and (c, d) $WO_{2.88}$-O_V with intercalated Li^+. The blue and purple regions represent the accumulation and dissipation of electron density, respectively.

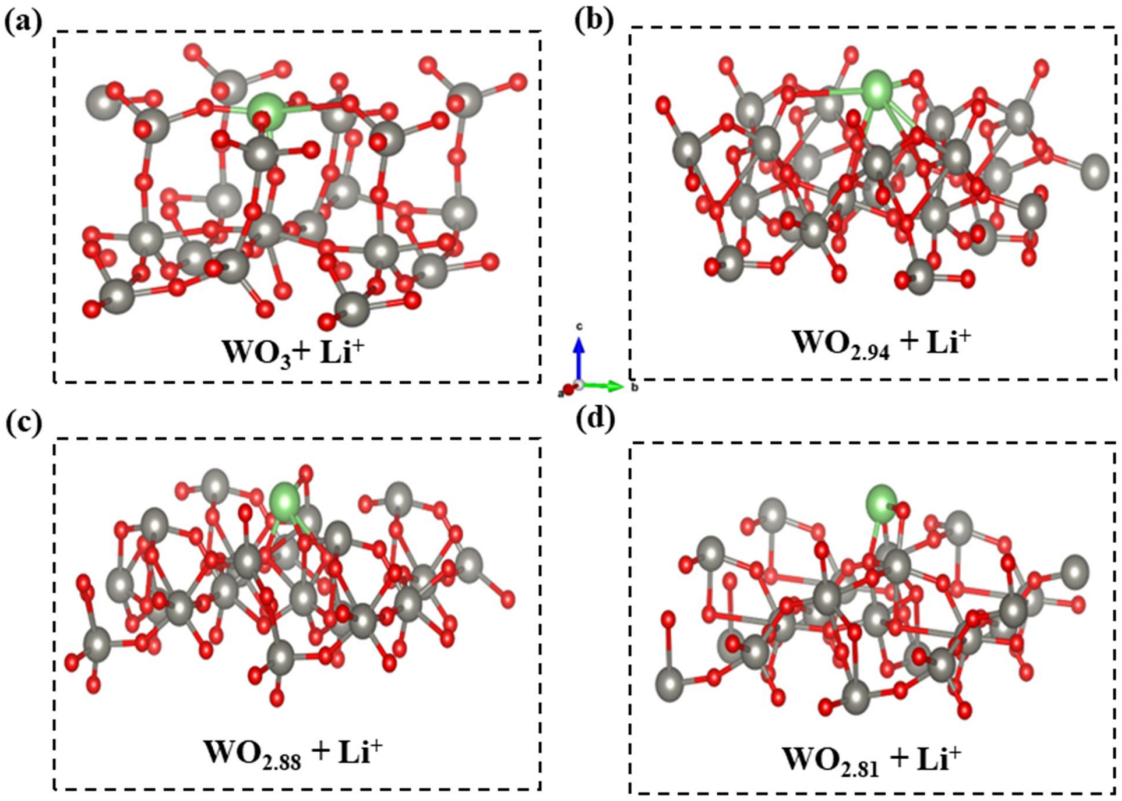

Fig. S11. Computational models (side view) of (a) pure WO_3 with intercalated Li^+, (b) $WO_{2.94}$-O_V with intercalated Li^+, (c) $WO_{2.88}$-O_V with intercalated Li^+ and (d) $WO_{2.81}$-O_V with intercalated Li^+.

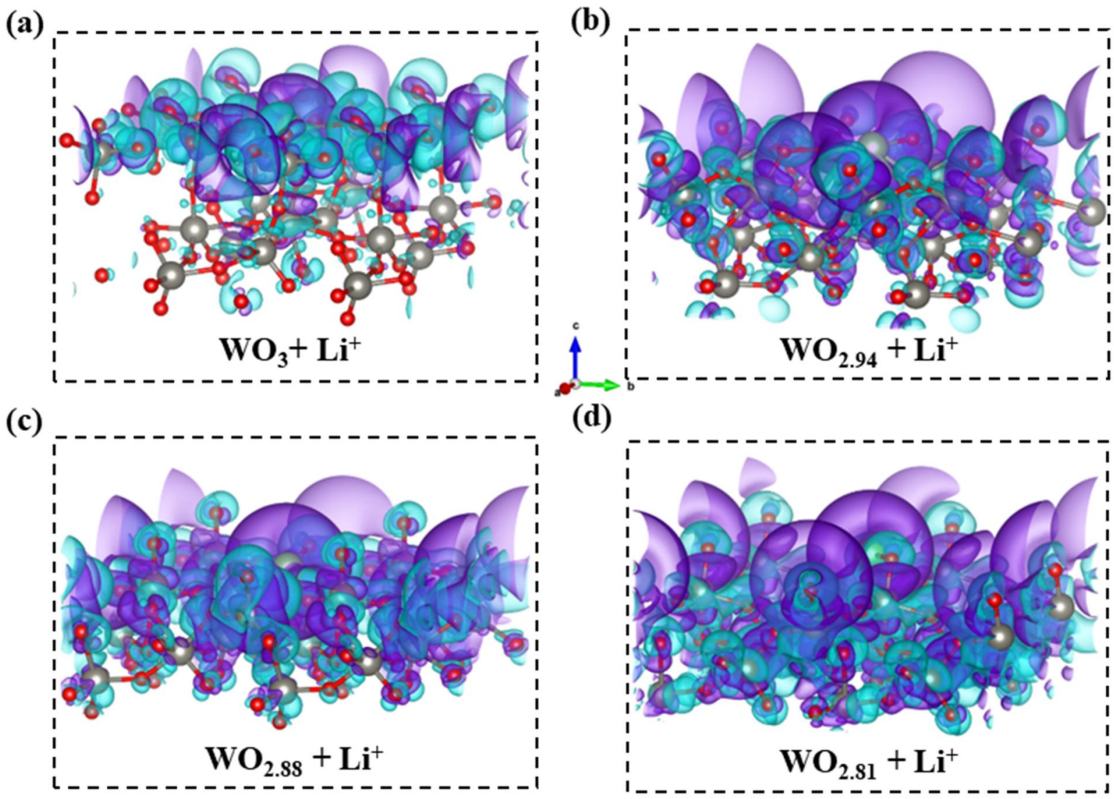

Fig. S12. Charge density difference (Side view) of (a) pure WO_3 with intercalated Li^+, (b) $WO_{2.94}$-O_V with intercalated Li^+, (c) $WO_{2.88}$-O_V with intercalated Li^+ and (d) $WO_{2.81}$-O_V with intercalated Li^+.

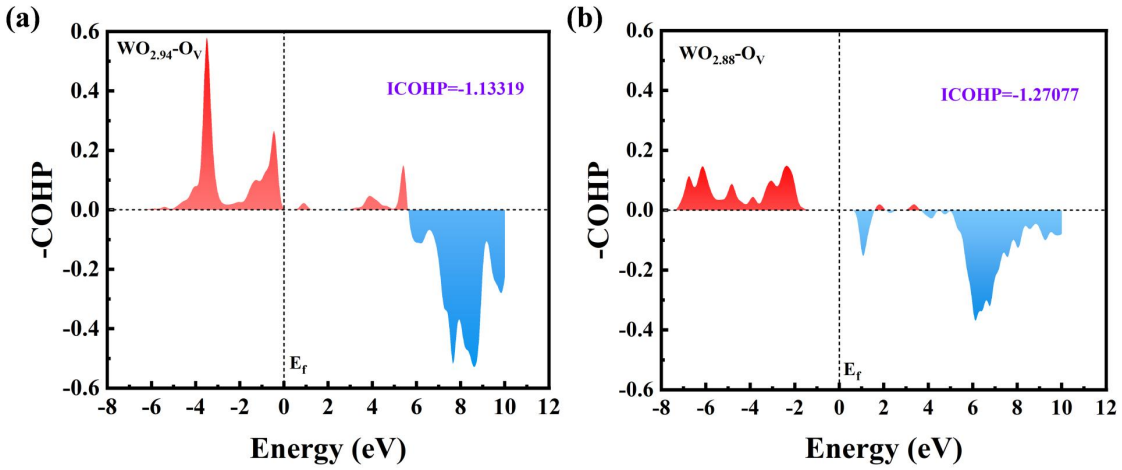

Fig. S13. The COHP between the Li and the O atoms in the (a) $WO_{2.94}$-O_V and (b) $WO_{2.88}$-O_V.

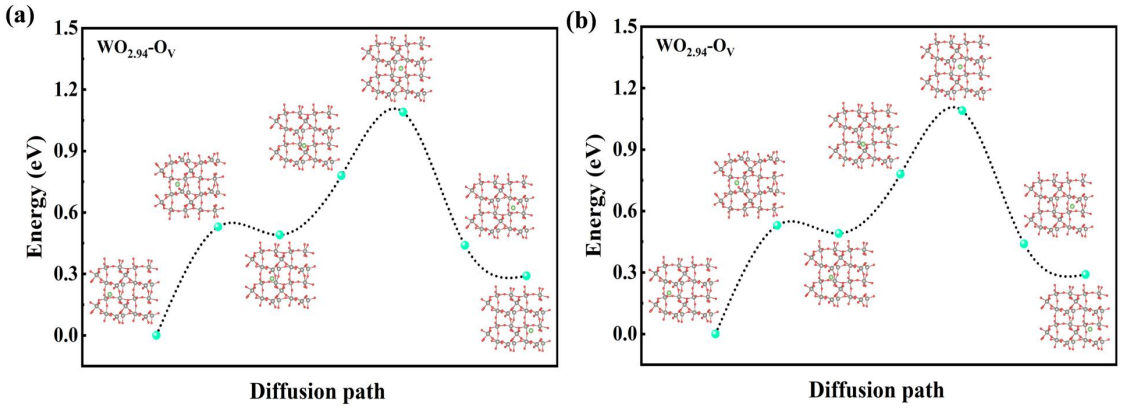

Fig. S14. The diffusion pathways of Li^+ and the corresponding diffusion energy barriers for (a) $WO_{2.94}$-O_V and (b) $WO_{2.88}$-O_V.

The initial optical transmission spectra of the a-WO_{3-x} films prepared at different oxygen flow rates were shown in **Fig. S15**. Initially, the pure WO_3 film without oxygen vacancy (a-WO_3-10) is highly transparent across the visible and NIR regions, and it has no absorption in the VIS light and NIR regions. In contrast, the oxygen vacancy modulated amorphous tungsten oxide (-WO_{3-x}-O_V-0, a-WO_{3-x}-O_V-2.5, a-WO_{3-x}-O_V-5, and a-WO_{3-x}-O_V-7.5) films show a broad absorption in the NIR region (800-1600 nm) with absorption intensity increasing as the oxygen mass flows decrease from 7.5 to 0 (**Fig. S15**). NIR extinction, a manifestation of the LSPR, is caused by an increase in the free electron concentration due to an increase in oxygen vacancy concentration in WO_{3-x} [13]. The inset of **Fig. S15** shows the digital photographs of a-WO_{3-x}-O_V-0, a-WO_{3-x}-O_V-2.5, a-WO_{3-x}-O_V-5, a-WO_{3-x}-O_V-7.5, and a-WO_3-10 films, the color of the WO_{3-x} films gradually change from transparent to blue with the decrease in the oxygen mass flow (the increase in oxygen vacancy concentration). Specifically, a-WO_{3-x}-O_V-0 film shows a poor visible light transmittance and a blue color, which indicating excessive oxygen vacancy will reduce the visible light transmittance, thereby do harm to the EC properties of the WO_{3-x} films [14].

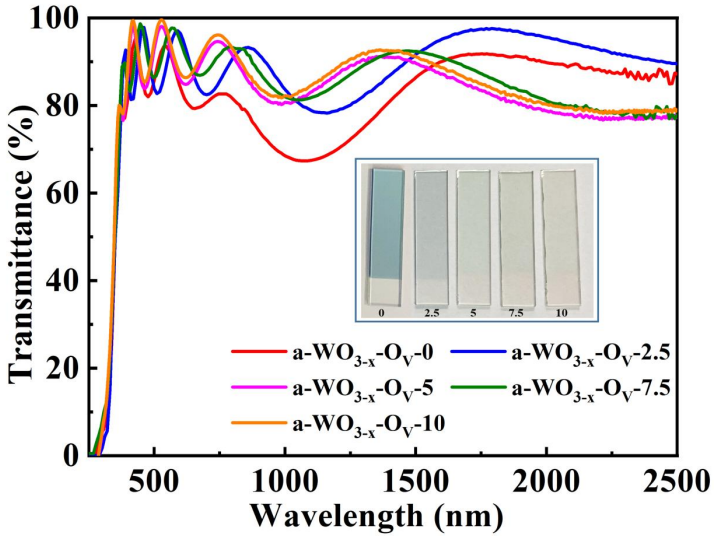

Fig. S15. The initial optical transmission spectra of the a-WO_{3-x} films prepared at different oxygen flow rates. Insets: digital photographs of the a-WO_{3-x} films prepared at different oxygen flow rates.

Fig. S16a-e show that the optical transmittance modulation of a-WO_{3-x}-O_V-0, a-WO_{3-x}-O_V-2.5, a-WO_{3-x}-O_V-5, a-WO_{3-x}-O_V-7.5, and a-WO_3-10 films at 633 nm are 86.5%, 91.8%, 87.5%, 85.8%, and 86.9%, respectively. These results indicate that a moderate oxygen vacancy level can significantly improve the electrochromic properties of WO_{3-x} films, and the a-WO_{3-x}-O_V-2.5 film has the largest optical transmittance modulation. The optical properties of a-WO_{3-x}-O_V-0 are worse than that of a-WO_{3-x}-O_V-2.5 because of the decrease in the transmittance of the bleached state, which may be attributed to the strong LSPR absorption caused by the excess oxygen vacancy in the a-WO_{3-x}-O_V-0 films [13, 14]. In addition, only the oxygen vacancy modulated amorphous tungsten oxide films (prepared at low O_2 flow rate) have the performance of selectively regulating VIS and NIR light transmittance, and they have a cold mode (-0.2 V): they can block more than 60% NIR solar heat while maintaining a more than 65% visible light transmittance. However, the pure WO_3 films without oxygen vacancy (a-WO_3-10) performed poorly in NIR selective modulation at -0.2 V, thereby validating the oxygen vacancy plays a crucial role in selective modulation of the VIS and NIR light transmittance.

The calculated CE values based on the **Equation S4-S6** are 106.89, 138.65, 117.71, 98.26 and 86.63 $cm^2 \cdot C^{-1}$ at 633 nm for the a-WO_{3-x}-O_V-0, a-WO_{3-x}-O_V-2.5, a-WO_{3-x}-O_V-5, a-WO_{3-x}-O_V-7.5, and a-WO_3-10 films, respectively (**Fig. S16f**), in which the a-WO_{3-x}-O_V-2.5 film exhibits the highest CE value. This is agreement well with the results of optical transmittance spectra, indicating that the a-WO_{3-x}-O_V-2.5 film shows the most excellent EC performance.

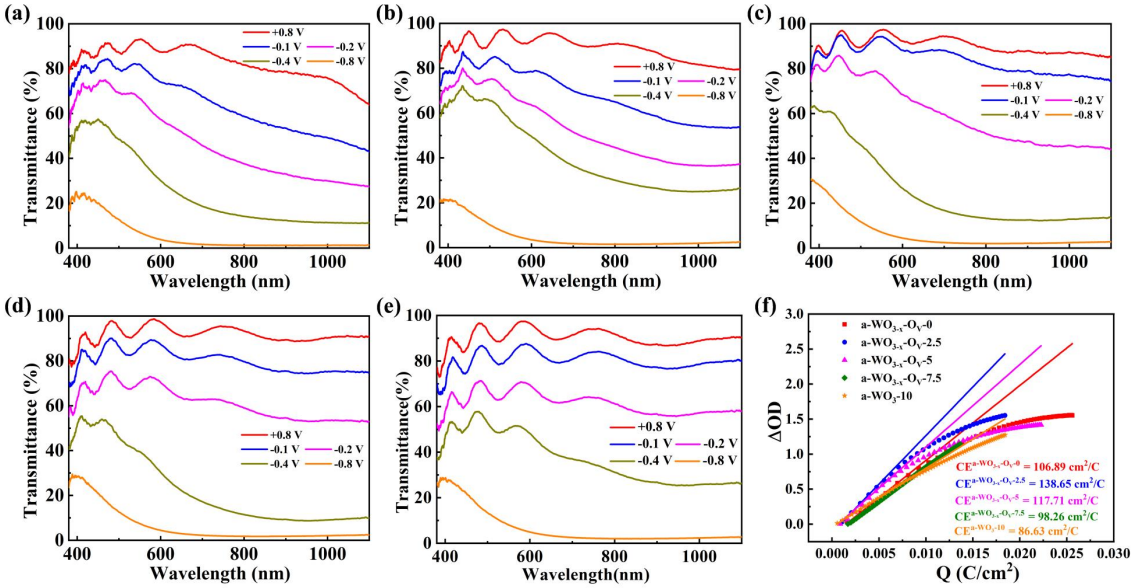

Fig. S16. Optical transmittance spectra of the (a) a-WO_{3-x}-O_V-0, (b) a-WO_{3-x}-O_V-2.5, (c) a-WO_{3-x}-O_V-5, (d) a-WO_{3-x}-O_V-7.5, and (e) a-WO_3-10 films under different applied potentials from +0.8 to −0.8 V Vs. Ag/AgCl. (f) Coloration efficiency (CE) of the a-WO_{3-x} films prepared at different oxygen flow rates.

Fig. S17a-e show the real-time transmittance spectra of a-WO_{3-x}-O_V-0, a-WO_{3-x}-O_V-2.5, a-WO_{3-x}-O_V-5, a-WO_{3-x}-O_V-7.5, and a-WO_3-10 films at 633 nm. It is observed that the response time of WO_{3-x} film gradually becomes longer with the decrease in the oxygen mass flows (the increase in oxygen vacancy concentration). The response speed of a-WO_{3-x}-O_V-0 (t_c= 2.5s, t_b= 3.5s) is the fastest, and the response speed of a-WO_3-10 (t_c= 6.8s, t_b= 9.3s) is the slowest. The faster kinetics of the a-WO_{3-x}-O_V-0 film can clearly be attributed to the multi-type transport channels of the amorphous film as well as the high conductivity and facilitated Li^+ diffusion paths in oxygen vacancy modulated WO_{3-x} films [15].

To further evaluate the influence of oxygen vacancy on Li^+ diffusion kinetic in the WO_{3-x} host, the Li^+ diffusion coefficients of the a-WO_{3-x}-O_V-0, a-WO_{3-x}-O_V-2.5, a-WO_{3-x}-O_V-5, a-WO_{3-x}-O_V-7.5, and a-WO_3-10 films are calculated by the Randles-Sevick equation [16] from the CV curves measured at different sweep rates (**Fig. S17f**), are 14.55×10^{-10}, 7.92×10^{-10}, 5.83×10^{-10}, 3.90×10^{-10} and 2.26×10^{-10}, respectively. Compared with the pure WO_3 films without oxygen vacancy (a-WO_3-10), the Li^+ diffusion coefficient in the oxygen vacancy-modulated amorphous tungsten oxide films (a-WO_{3-x}-O_V) are significant higher, which indicates that oxygen vacancy can facilitate Li^+ diffusion in the WO_{3-x} host to improve switching kinetics of the a-WO_{3-x}-O_V films.

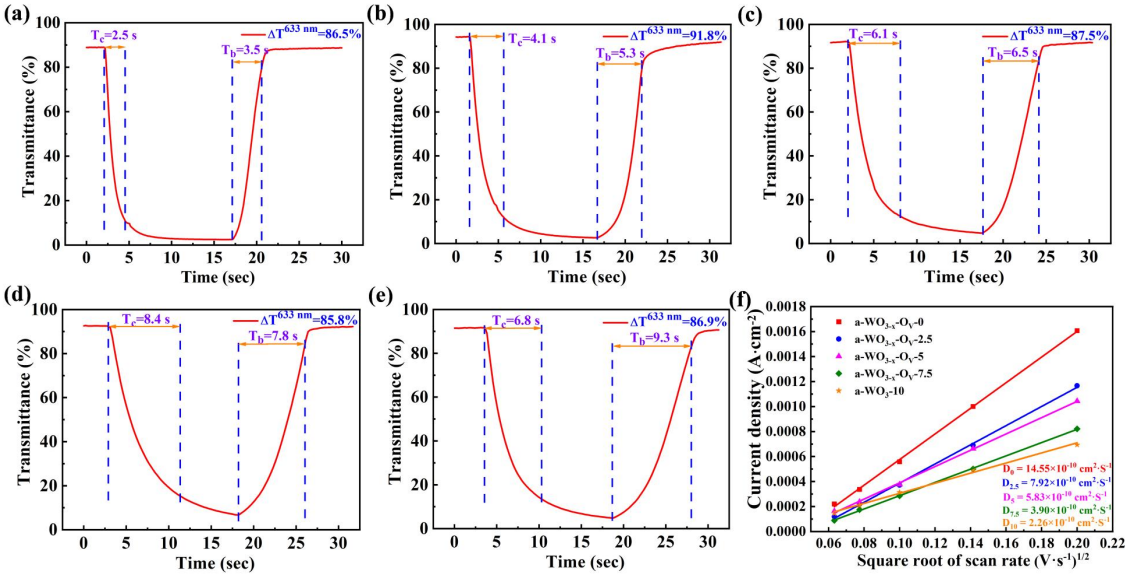

Fig. S17. Real-time transmittance spectra of the (a) a-WO_{3-x}-O_V-0, (b) a-WO_{3-x}-O_V-2.5, (c) a-WO_{3-x}-O_V-5, (d) a-WO_{3-x}-O_V-7.5, and (e) a-WO_3-10 films at 633 nm. (f) The peak anodic current density as functions of square roots of scan rates for the a-WO_{3-x} films prepared at different oxygen flow rates.

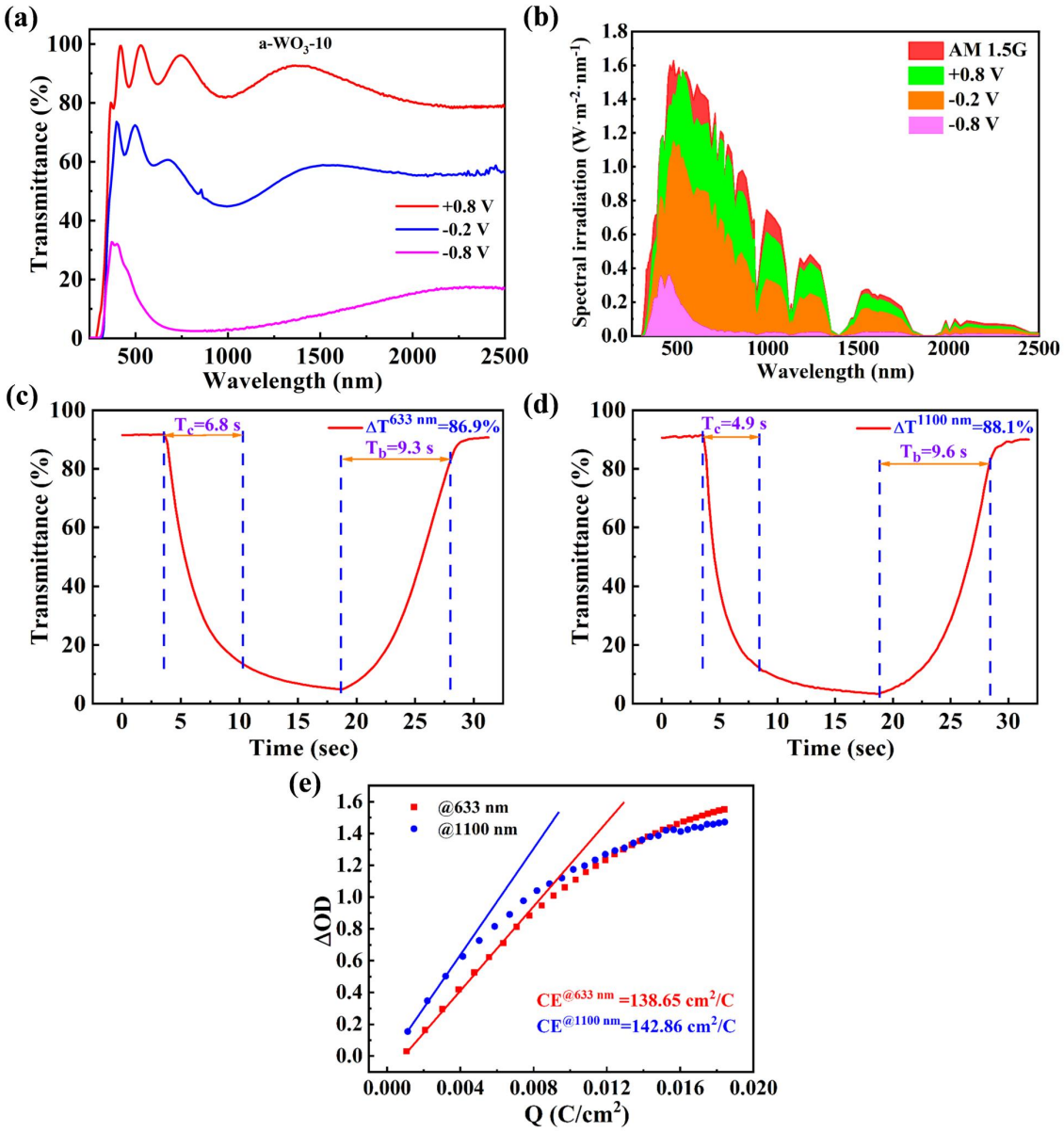

Fig. S18. Electrochromic properties of the a-WO_3-10 film. (a) Optical transmission spectra and (b) corresponding solar irradiance spectra of the a-WO_3-10 film. (c, d) Real-time transmittance spectra of the a-WO_3-10 film at (c) 633 nm and (d) 1100 nm. (e) Coloration efficiency (CE) of the a-WO_3-10 film at 633 and 1100 nm.

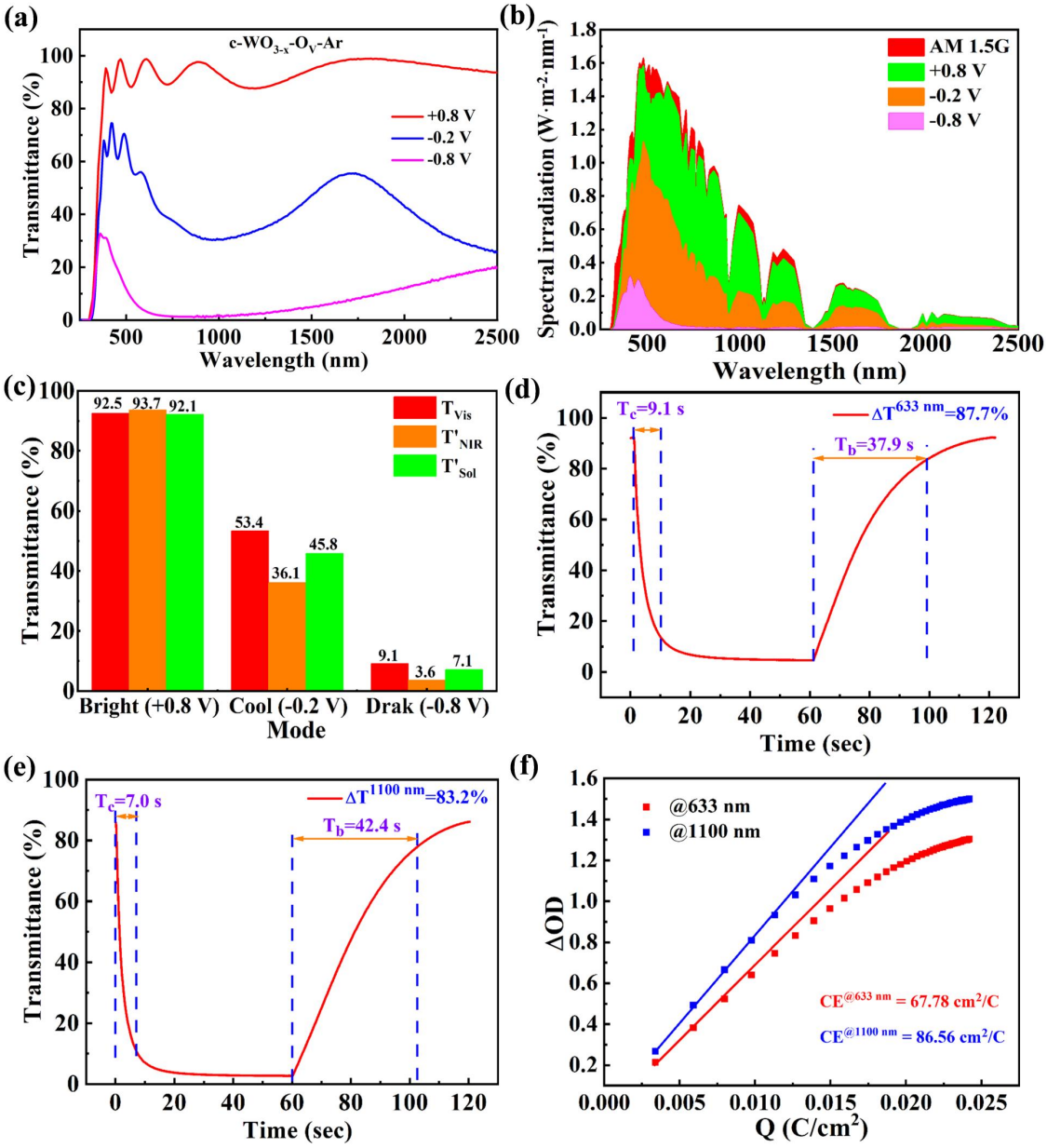

Fig. S19. Electrochromic properties of the c-WO_{3-x}-O_V-Ar film. (a) Optical transmission spectra, (b) solar irradiance spectra, and (c) corresponding integrated optical transmittance (T) and integrated solar irradiance transmittance of the a-WO_3 film. Real-time transmittance spectra of the c-WO_{3-x}-O_V-Ar film at (d) 633 nm and (e) 1100 nm. (f) Coloration efficiency (CE) of the c-WO_{3-x}-O_V-Ar film at 633 and 1100 nm.

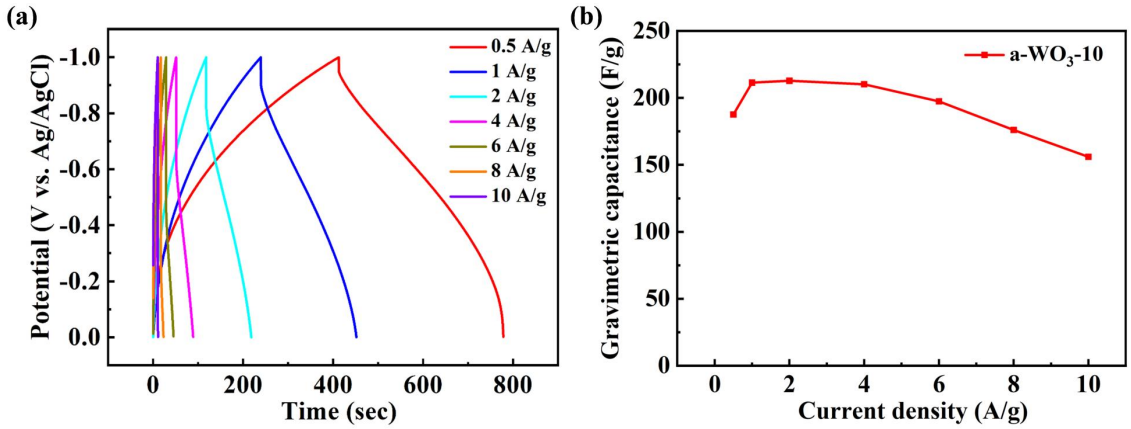

Fig. S20. Energy storage performance of the a-WO_3-10 film. (a) GCD curves and (b) specific capacitance as a function of the current density for the a-WO_3 -10 film at current densities ranging from 0.5 to 10 A g^{-1}.

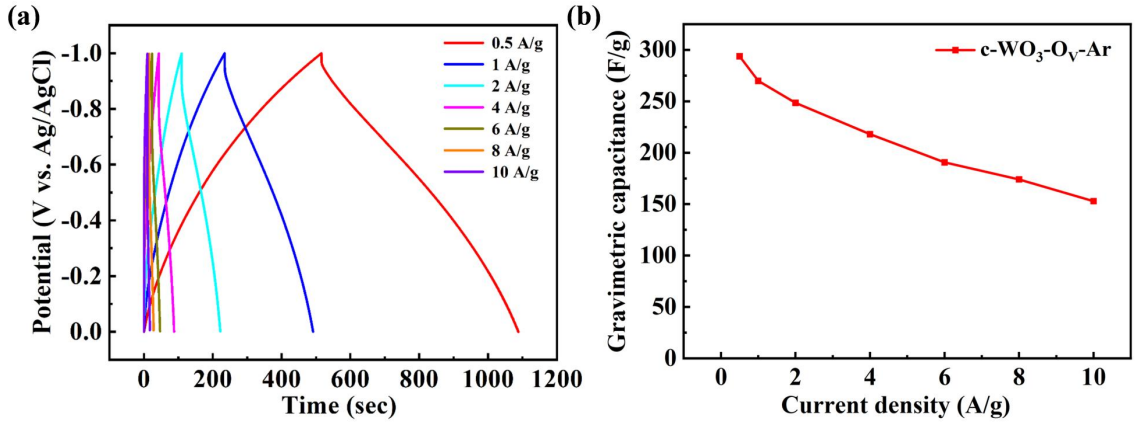

Fig. S21. Energy storage performance of the c-WO_{3-x}-O_V-Ar film. (a) GCD curves and (b) specific capacitance as a function of the current density for the c-WO_{3-x}-O_V-Ar film at current densities ranging from 0.5 to 10 A g^{-1}.

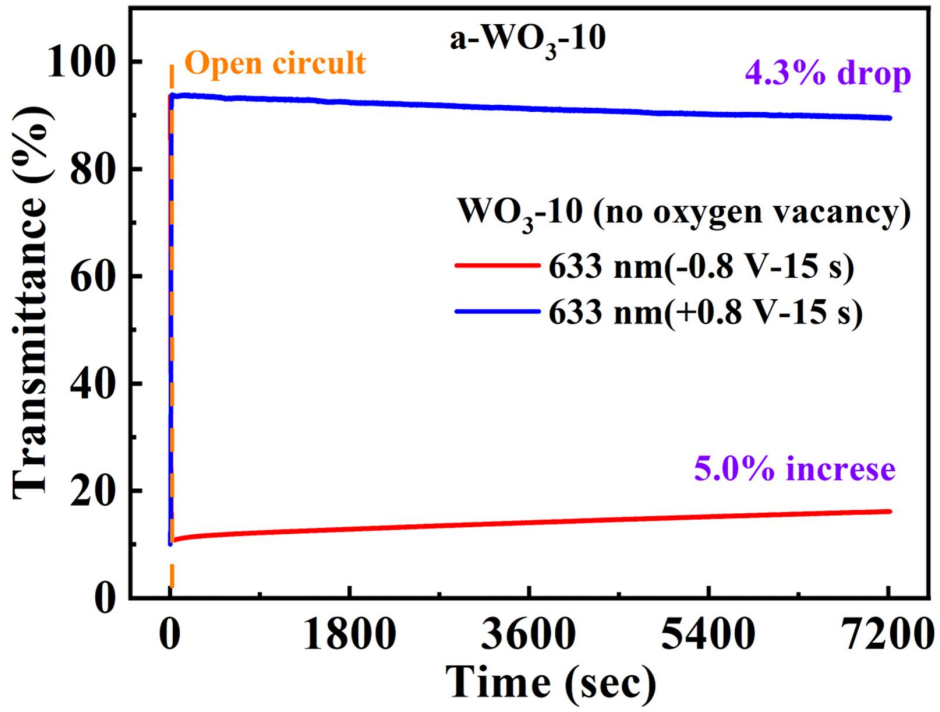

Fig. S22. Transmittance changes at 633 nm of the a-WO_3-10 film under the open-circuit condition after the applied potential is removed for 7200 s.

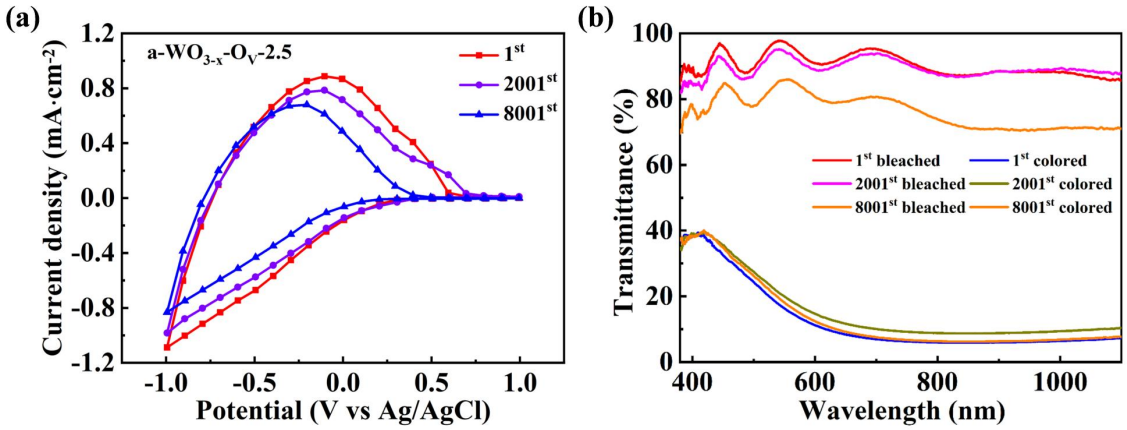

Fig. S23. (a) CV curves and (b) optical transmittance spectra of a-WO_{3-x}-O_v-Ar film during 8000 cycles.

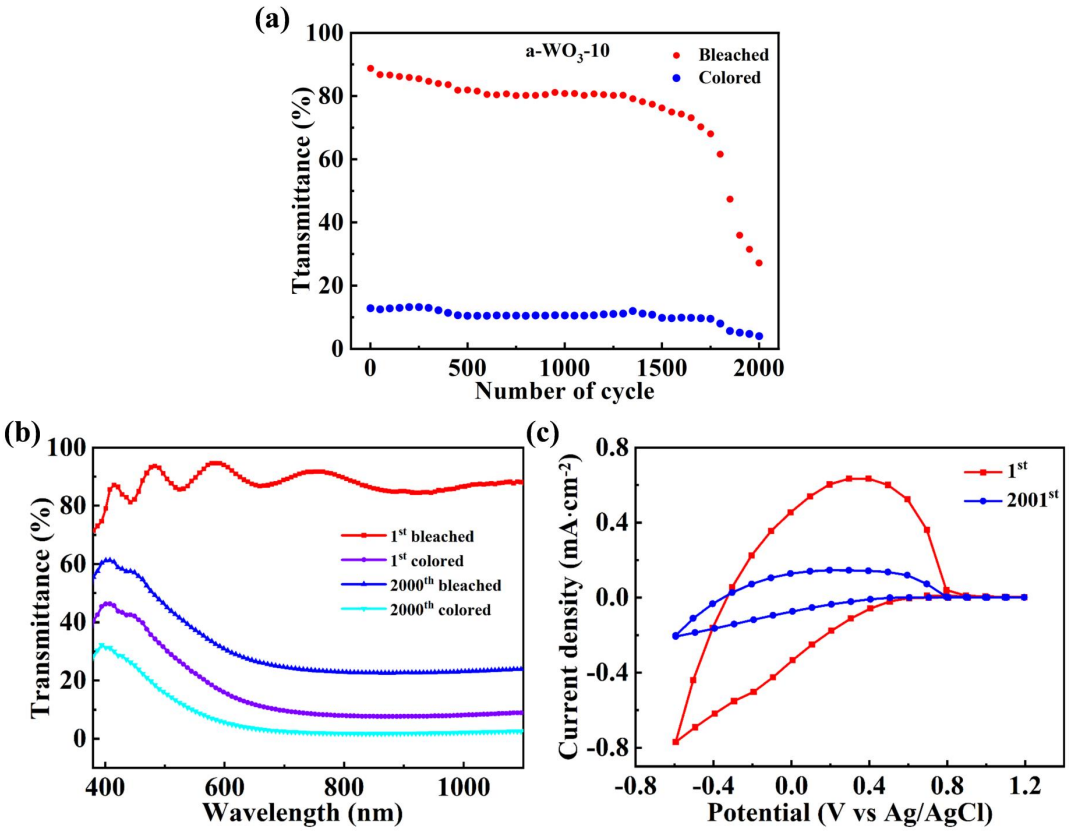

Fig. S24. Cycling performance of the a-WO_3-10 film. (a) *In situ* optical transmittance at a wavelength of 633 nm, (b) CV curves, and (c) optical transmittance spectra for the a-WO_3-10 film during 2000 cycles.

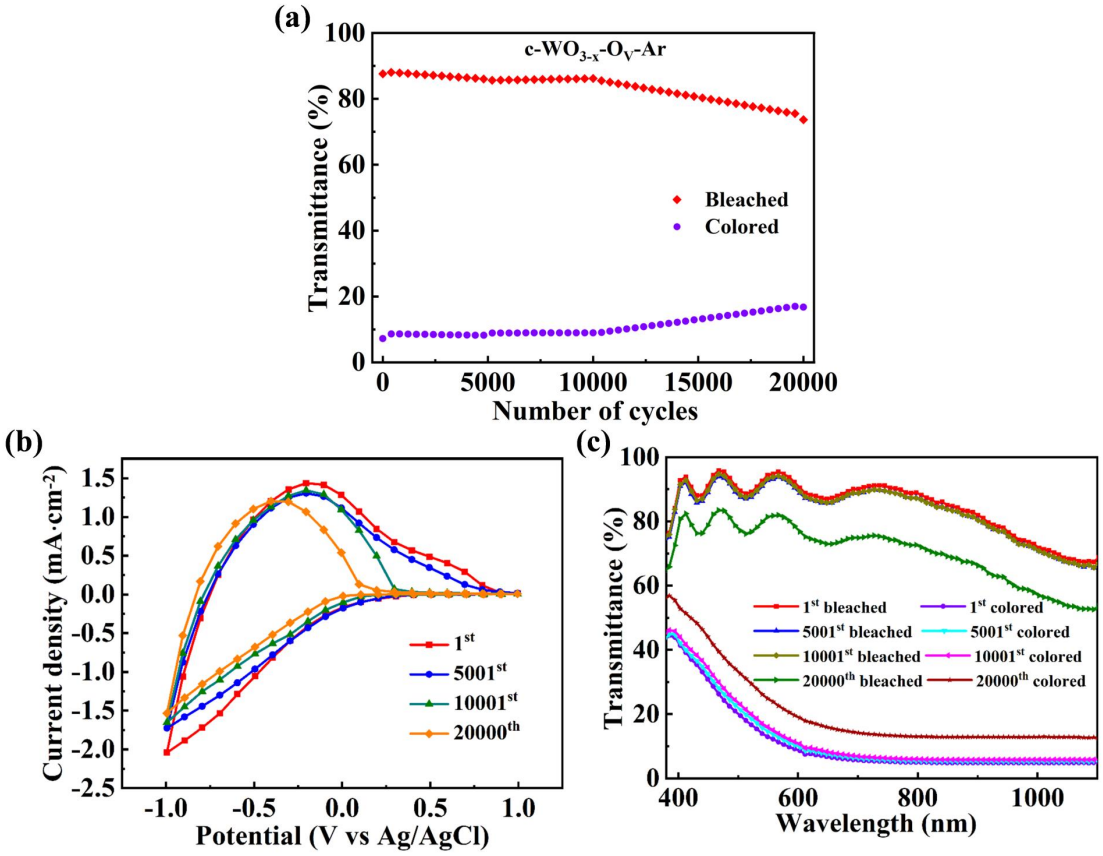

Fig. S25. Cycling performance of the c-WO_{3-x}-O_V-Ar film. (a) *In situ* optical transmittance at a wavelength of 633 nm, (b) CV curves, and (c) optical transmittance spectra for the c-WO_{3-x}-O_V-Ar film during 20000 cycles.

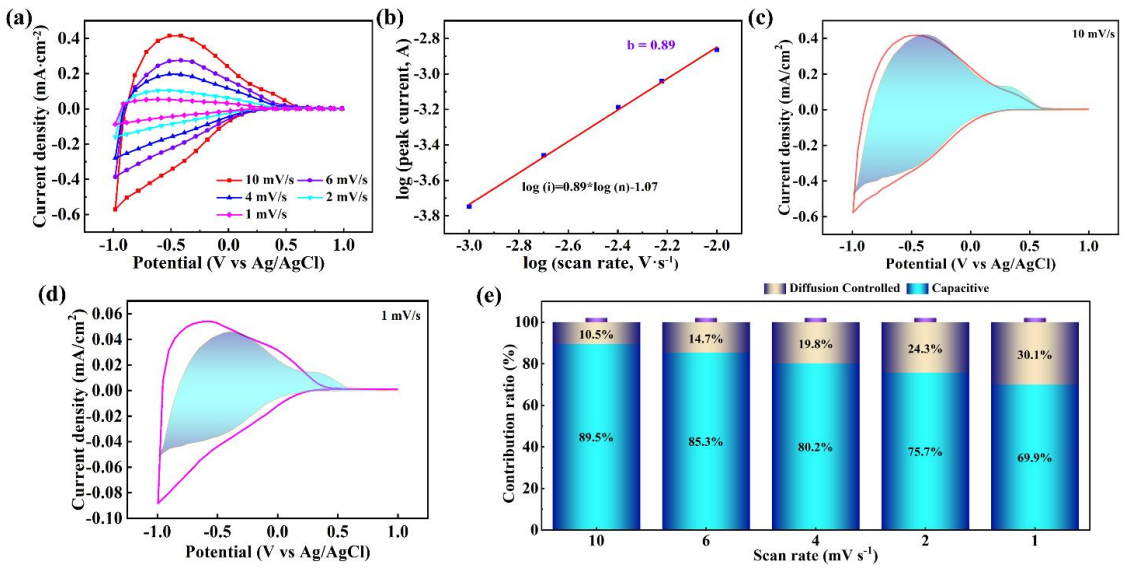

Fig. S26 Study on the electrochemical mechanism of the a-WO_{3-x}-O_V-2.5 film. (a) CV curves recorded at scan rates ranging from 10 to 1 mV/s. (b) Log (peak current) versus log (scan rate) plots according to the CV data at the oxidation peak. CV curves with the capacitive contribution (shadow area) at scan rates of (c) 10 and (d) 1 mV/s. (e) Percentage of diffusion-controlled and surface capacitive behavior at different scan rates.

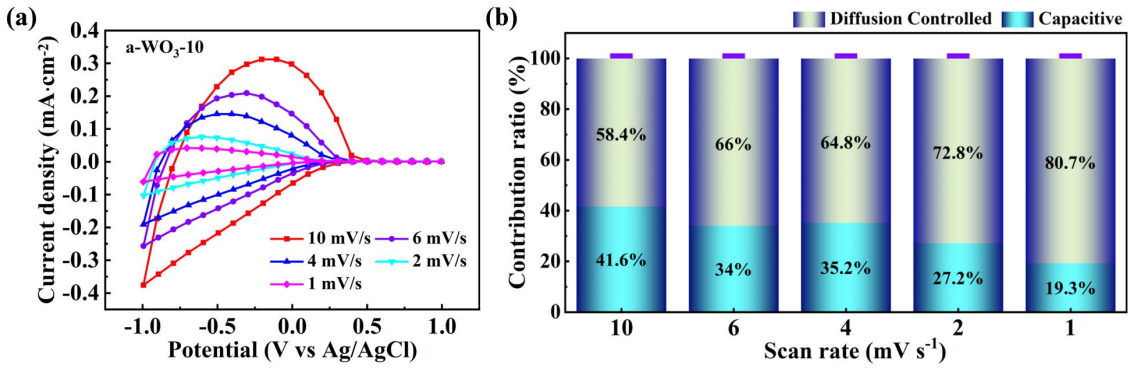

Fig. S27. (a) CV curves recorded at scan rates ranging from 10 to 1 mV/s and (b) percentage of diffusion-controlled and surface capacitive behavior at different scan rates for the a-WO_3-10 film.

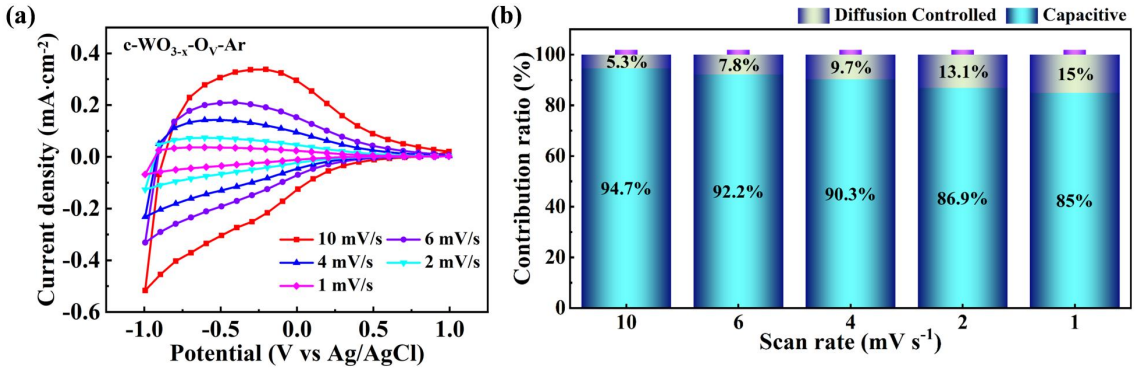

Fig. S28 (a) CV curves recorded at scan rates ranging from 10 to 1 mV/s and (b) percentage of diffusion-controlled and surface capacitive behavior at different scan rates for the c-WO_{3-x}-O_V-Ar film.

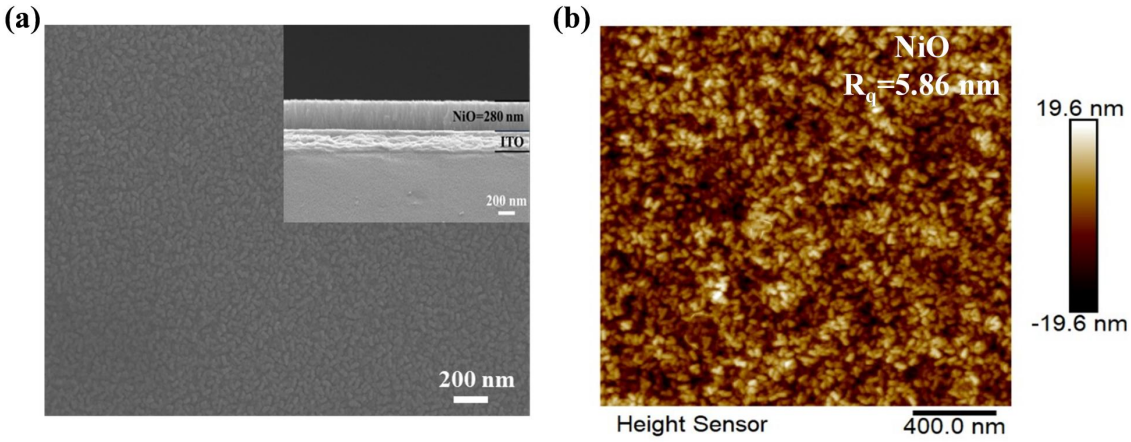

Fig. S29. (a) SEM image (Inset: cross-sectional SEM image) and (b) AFM image of the NiO film.

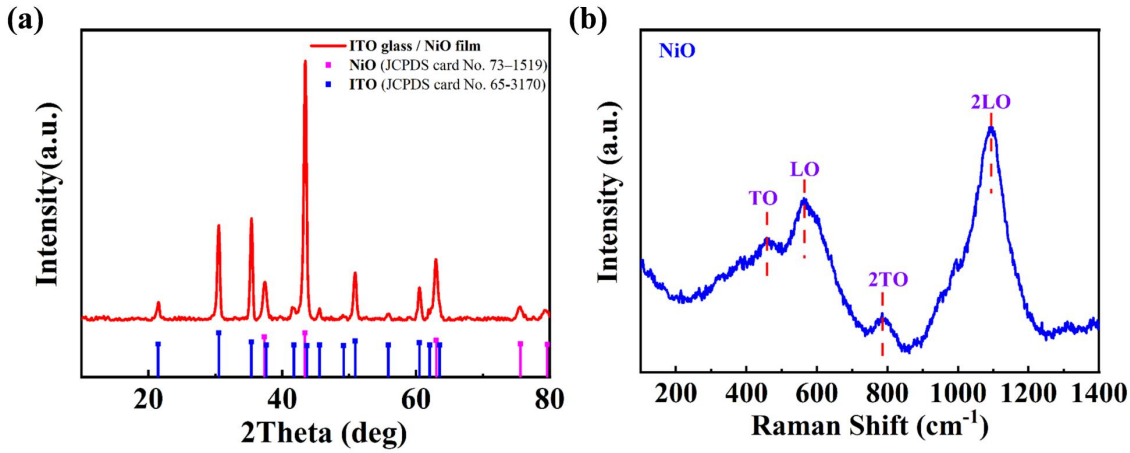

Fig. S30. (a) XRD pattern and (b) Raman spectrum of the NiO film.

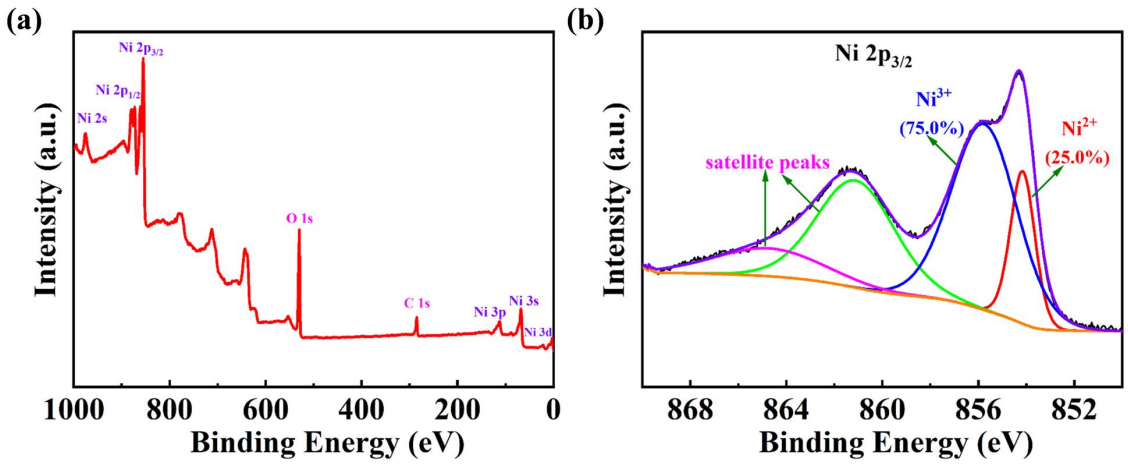

Fig. S31. (a) XPS survey spectrum and (b) high-resolution Ni 2p XPS spectrum of the NiO film.

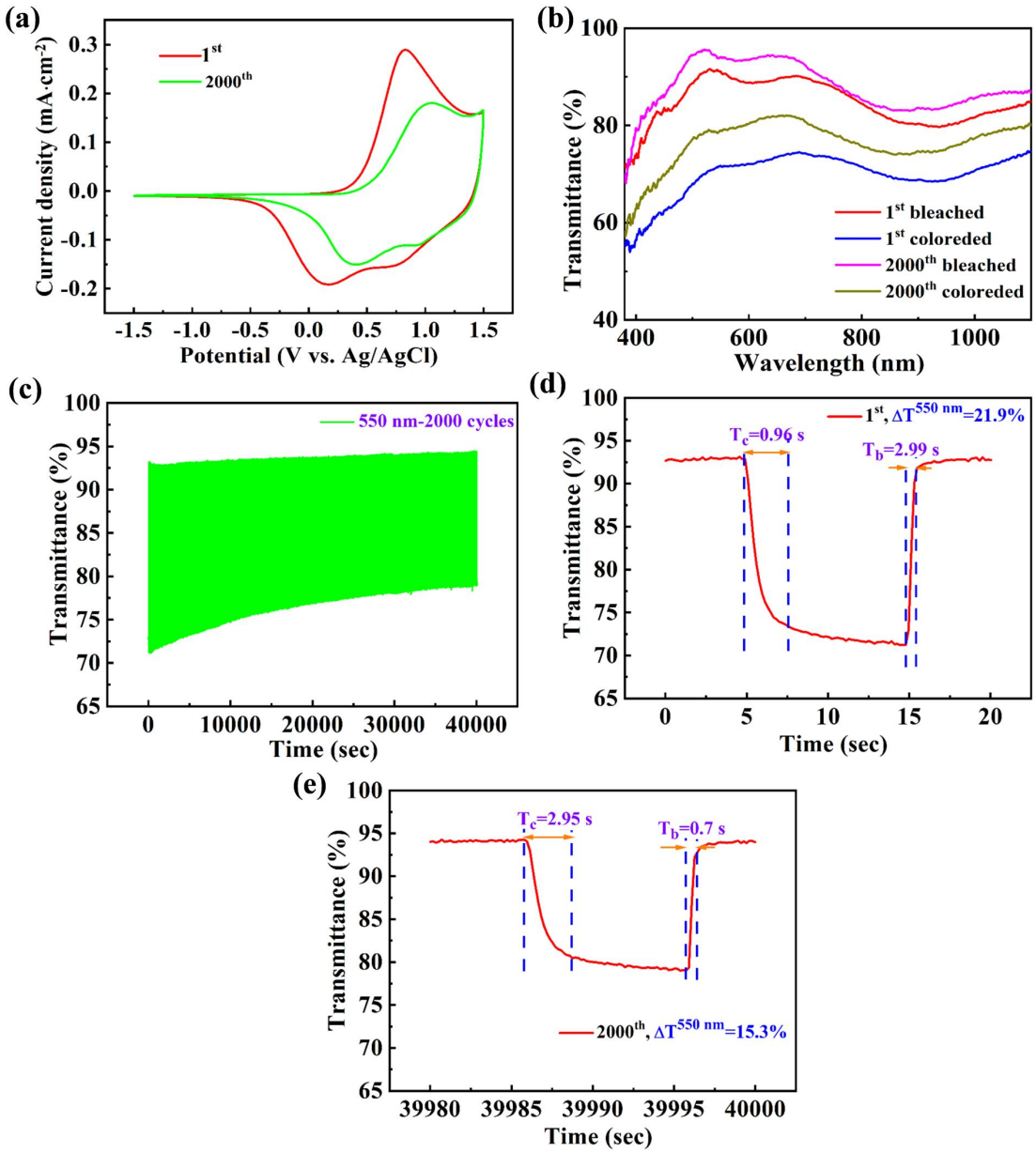

Fig. S32. Electrochemical and electrochromic properties of the NiO film. (a) CV curves, (b) optical transmittance spectra, and (c) *in situ* optical transmittance at a wavelength of 550 nm during 2000 cycles. (d, e) Real-time transmittance spectra at a wavelength of 633 nm during (d) 1st and (e) 2000th cycle.

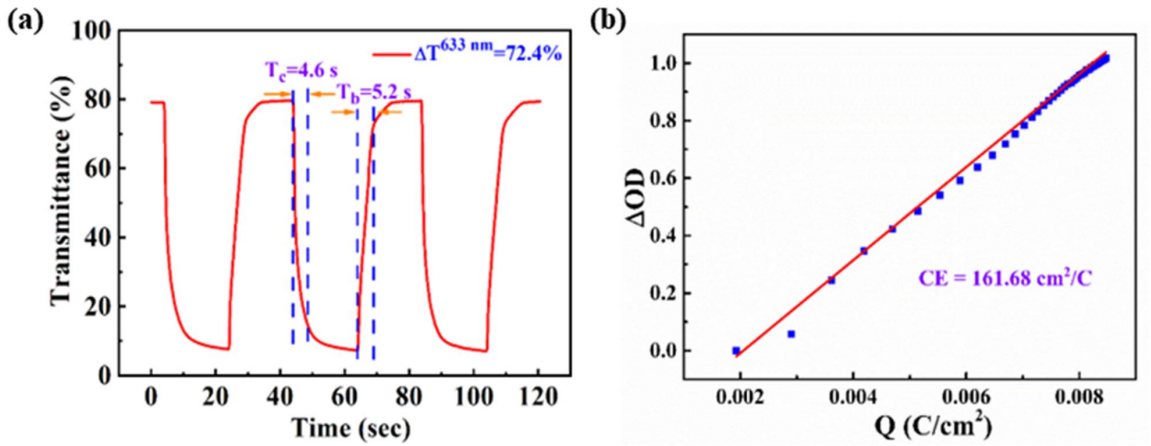

Fig. S33. Electrochromic performance of the demonstrative DEES device. (a) Real-time transmittance spectra and (b) coloration efficiency at a wavelength of 633 nm.

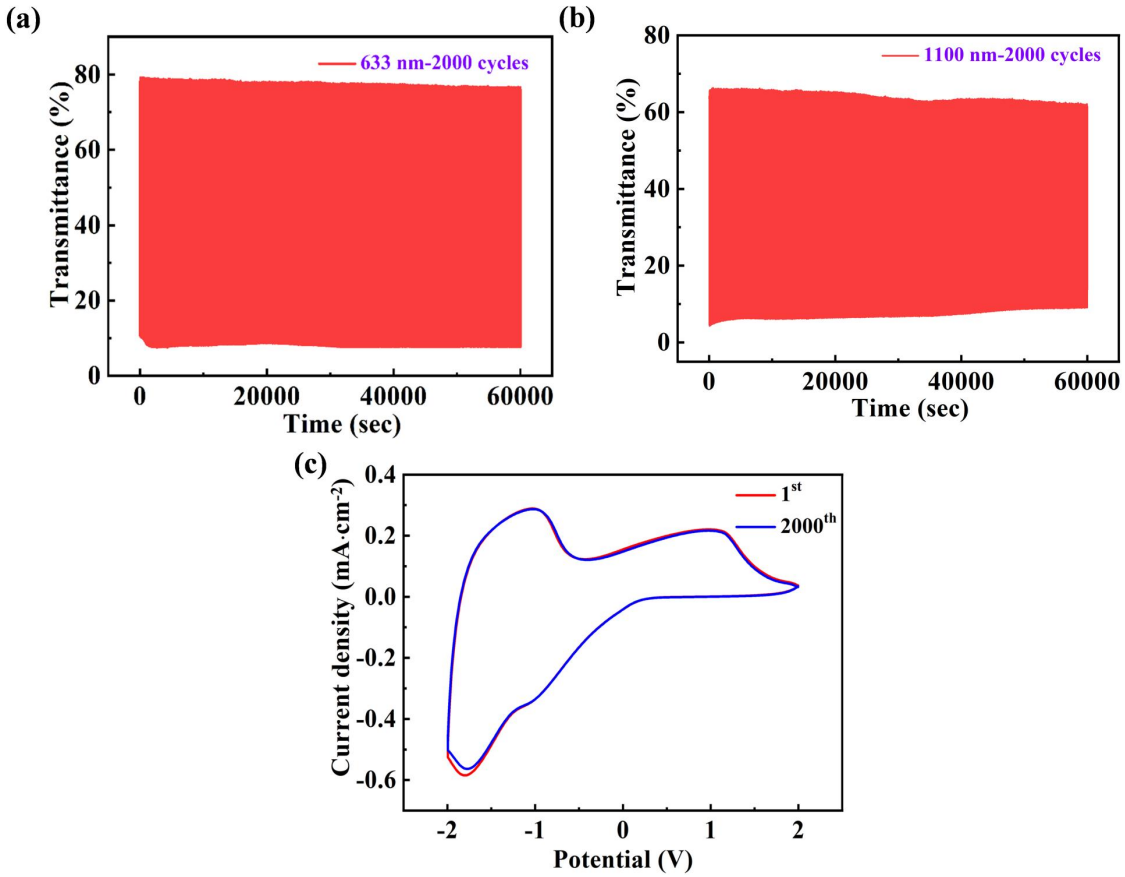

Fig. S34. Cycling performance of the demonstrative DEES device. (a) In situ optical transmittance at a wavelength of 633 nm during 2000 cycles, and (d) CV curves before and after 2000 cycles.

Tables

Table S1. The detailed parameters during the preparation process of WO_{3-x} films.

Samples	Mass flows of O_2 (sccm)	Pressure of the chamber (Pa)	Deposition rate (nm/s)	Deposition temperature (℃)	Thickness of the thickness monitor (Å)
a-WO_{3-x}-O_v-0	0	1.0×10^{-5}	0.15-0.25	200	1650
a-WO_{3-x}-O_v-2.5	2.5	8.5×10^{-3}	0.15-0.25	200	1650
a-WO_{3-x}-O_v-5	5	1.0×10^{-2}	0.15-0.25	200	1650
a-WO_{3-x}-O_v-7.5	7.5	1.5×10^{-2}	0.15-0.25	200	1650
a-WO_3-10	10	2.1×10^{-2}	0.15-0.25	200	1650
c-WO_{3-x}-O_v-Ar	2.5	8.8×10^{-3}	0.15-0.25	200	1650

Table S2. Comparison of electrochromic performance (optical modulation (**Δ**T), switching time (t_b/t_c), coloration efficiency (CE), specific capacitance and cycling stability) of our works and those current state-of-the-art dual-band electrochromic materials. N/A indicates data is not available.

Samples	**Δ**T (%)	t_b/t_c (s)	CE (cm^2/C)	capacitance ($F \cdot g^{-1}$)	Cycling stability
ITO-NbO_x [17]	~35% (633 nm)	N/A	30 ±4 (500 nm)	N/A	2000 (retain 96%)
ITO-NbO_x [18]	~40% (633 nm)	N/A	N/A	N/A	2000 (retain 95%)
WO_{3-x}-NbO_x [19]	~80% (633 nm)	600/100	N/A	N/A	2000 (retain 94.3%)
$W_{18}O_{49}$/PB [20]	71.2% (633 nm)	2.4/4.2	N/A	N/A	100 (retain 98.3%)
Nd-Mo-SnO_2/a-WO_3 [21]	~31.9 (600 nm)	~17.5/~4.2	198.8	N/A	900 (retain 875%)
Nb-TiO_2 [22]	~76% (633 nm)	105/~10	N/A	N/A	200
Nb-TiO_2 [23]	37.75 (600 nm)	25/5	N/A	N/A	1000
Ta-TiO_2 [24]	89.1 (550 nm)	9.5/52.6	29.7 (550	183 $mAh \cdot g^{-1}$ at	2000 (retain

			nm)	0.2 A·g^{-1}	99.8%)
TiO_{2-x} [14]	95.5 (633 nm)	9.6/35.1	38.2 (633 nm)	N/A	2000 (retain 95.6%)
$Nb_{12}O_{29}$ NPLs [25]	~75 (600 nm)	N/A	136 (550nm)	N/A	500 (retain ~67%)
$Nb_{18}W_{16}O_{93}$ [26]	93 (633 nm), 89 (1200 nm)	10.1/12.7	105.6 (633 nm)	151.4 mAh·g^{-1} at 2 A· g^{-1}	6000 (retain 66.4%)
WO_3 SNRs [2]	~82 (633 nm)	98/>1200	21 (600nm)	N/A	200 (retain 84%)
m-WO_3 NWs [27]	91.7 (633 nm)	21/85	101.7 (633 nm)	N/A	1000 (retain 91.7%)
a-WO_{3-x}-O_v (Our work)	**91.8 (633 nm)**	**4.1/5.3**	**167.96 (1100 nm)**	**314 F·g^{-1} at 0.5 A·g^{-1}**	**8000 (retain 83.3%)**

N/A indicates data is not available.

Table S3. The oxygen vacancy concentration and EC performance (optical modulation, switching time, coloration efficiency (CE), specific capacitance and cycling stability) of WO_{3-x} films. The t_c/t_b indicate the coloration/bleaching time. The calculation of optical modulation (ΔT) is based on Eq. S2 and S3.

Samples	Oxygen vacancy concentration (%)	**Δ**T (%) at 633 nm	t_b/t_c (s)	CE (cm^2/C)	specific capacitance ($F \cdot g^{-1}$)	Cycling stability
a-WO_3-5	0	86.9	6.8/9.3	142.86	187.6 $F \cdot g^{-1}$ at 0.5 $A \cdot g^{-1}$	2000 (retain 30.4%)
a-WO_{3-x}-O_v-2.5	**4.33**	**91.8**	**4.1/5.3**	**167.96**	**314 $F \cdot g^{-1}$** at 0.5 $A \cdot g^{-1}$	**8000 (retain 83.3%)**
c-WO_{3-x}-O_V-Ar	6.65	87.7	9.1/37.9	86.56	293.7 $F \cdot g^{-1}$ at 0.5 $A \cdot g^{-1}$	20000 (retain 70.8%)

Table S4. Integrated optical transmittance (T) and integrated solar irradiance transmittance (T') of the demonstrative DEES device in the VIS light (380-780 nm), NIR (780-2500 nm; and total solar irradiation (sol, 300-2500 nm) at +2.0, -1.2, and -2.0 V.

Mode	T_{VIS}	T_{NIR}	T_{sol}	T'_{VIS}	T'_{NIR}	T'_{sol}
Bright (+2.0 V)	**81.0%**	64.0%	66.1%	81.3%	**69.5%**	**75.1%**
Cool (-1.2 V)	**57.6%**	32.0%	35.1%	58.1%	**31.4%**	**46.2%**
Dark (-2.0 V)	**4.5%**	4.0%	4.2%	4.5%	**2.5%**	**3.7%**

References

1. J. Wang, J. Polleux, J. Lim and B. Dunn, *J. Phys. Chem. C*, 2007, **111**, 14925-14931.
2. R. Giannuzzi, R. Scarfiello, T. Sibillano, C. Nobile, V. Grillo, C. Giannini, P. D. Cozzoli and M. Manca, *Nano Energy*, 2017, **41**, 634-645.
3. Q. Zhao, J. Wang, X. Ai, Y. Duan, Z. Pan, S. Xie, J. Wang and Y. Gao, *InfoMat*, 2022, **4**, e12298.
4. Z. Luo, L. Liu, X. Yang, X. Luo, P. Bi, Z. Fu, A. Pang, W. Li and Y. Yi, *ACS Appl. Mater. Interfaces*, 2020, **12**, 39098-39107.
5. C. Deng, K. Zhang, L. Liu, Z. He, J. Huang, T. Wang, Y. Liu, X. He, K. Du and Y. Yi, *J. Mater. Chem. A*, 2022, **10**, 17326-17337.
6. M. Chen, X. Zhang, W. Sun, W. Li, Y. Zhao, Z. Li, Y. Xiao, J. Wang, Y. Li and J. Zhao, *Electrochim. Acta*, 2022, **431**, 141101.
7. Y. Zhao, X. Zhang, W. Li, Z. Li, H. Zhang, M. Chen, W. Sun, Y. Xiao, J. Zhao and Y. Li, *Sol. Energy Mater Sol. Cells*, 2022, **237**, 111564.
8. S.-H. Lee, M. J. Seong, H. M. Cheong, E. Ozkan, E. C. Tracy and S. K. Deb, *Solid State Ion*, 2003, **156**, 447-452.
9. Y. Zhao, X. Zhang, X. Chen, W. Li, L. Wang, F. Ren, J. Zhao, F. Endres and Y. Li, *ACS Sustain. Chem. Eng.*, 2020, **8**, 11658-11666.
10. J. Wan, J. Xu, S. Zhu, J. Li, G. Ying, B. Wang and K. Chen, *Chem. Eng. J.*, 2022, **444**, 136604.
11. Z. Wei, W. Wang, W. Li, X. Bai, J. Zhao, E. C. M. Tse, D. L. Phillips and Y. Zhu, *Angew. Chem. Int. Ed.*, 2021, **60**, 8236-8242.
12. N. Zhang, X. Li, H. Ye, S. Chen, H. Ju, D. Liu, Y. Lin, W. Ye, C. Wang, Q. Xu, J. Zhu, L. Song, J. Jiang and Y. Xiong, *J. Am. Chem. Soc.*, 2016, **138**, 8928-8935.
13. C. J. Dahlman, Y. Tan, M. A. Marcus and D. J. Milliron, *J. Am. Chem. Soc.*, 2015, **137**, 9160-9166.

14. S. Zhang, S. Cao, T. Zhang and J. Y. Lee, *Adv. Mater.*, 2020, **32**, e2004686.

15. C. Chen, H. Zhu, M. Shi, L. Hu, Z. Xue, H. Ye, L. Zhao and C. Yan, *Energy Stor. Mater.*, 2022, **49**, 370-379.

16. R. Li, X. Ma, J. Li, J. Cao, H. Gao, T. Li, X. Zhang, L. Wang, Q. Zhang, G. Wang, C. Hou, Y. Li, T. Palacios, Y. Lin, H. Wang and X. Ling, *Nat. Commun.*, 2021, **12**, 1587.

17. A. Llordes, G. Garcia, J. Gazquez and D. J. Milliron, *Nature*, 2013, **500**, 323-326.

18. A. Llordes, Y. Wang, A. Fernandez-Martinez, P. Xiao, T. Lee, A. Poulain, O. Zandi, C. A. Saez Cabezas, G. Henkelman and D. J. Milliron, *Nat. Mater.*, 2016, **15**, 1267-1273.

19. J. Kim, G. K. Ong, Y. Wang, G. LeBlanc, T. E. Williams, T. M. Mattox, B. A. Helms and D. J. Milliron, *Nano Lett.*, 2015, **15**, 5574-5579.

20. Z. Wang, Q. Zhang, S. Cong, Z. Chen, J. Zhao, M. Yang, Z. Zheng, S. Zeng, X. Yang, F. Geng and Z. Zhao, *Adv. Opt. Mater.*, 2017, **5**, 1700194.

21. R. Goei, A. J. Ong, T. J. Hao, L. J. Yi, L. S. Kuang, D. Mandler, S. Magdassi and A. I. Yoong Tok, *Ceram. Int.*, 2021, **47**, 18433-18442.

22. M. Barawi, L. De Trizio, R. Giannuzzi, G. Veramonti, L. Manna and M. Manca, *ACS Nano*, 2017, **11**, 3576-3584.

23. R. Liu, Y. Ren, J. Wang, Y. Wang, J. Jia and G. Zhao, *Ceram. Int.*, 2021, **47**, 31834-31842.

24. S. Cao, S. Zhang, T. Zhang, Q. Yao and J. Y. Lee, *Joule*, 2019, **3**, 1152-1162.

25. H. C. Lu, S. Ghosh, N. Katyal, V. S. Lakhanpal, I. R. Gearba-Dolocan, G. Henkelman and D. J. Milliron, *ACS Nano*, 2020, **14**, 10068-10082.

26. G. Cai, R. Zhu, S. Liu, J. Wang, C. Wei, K. J. Griffith, Y. Jia and P. S. Lee, *Adv. Energy Mater.*, 2021, **12**, 2103106.

27. S. Zhang, S. Cao, T. Zhang, Q. Yao, A. Fisher and J. Y. Lee, *Mater. Horizons*, 2018, **5**, 291-297.